NASADEM

S. M. Buckley, P. S. Agram, J. E. Belz, R. E. Crippen, E. M. Gurrola, S. Hensley, M. Kobrick, M. Lavalle, J. M. Martin, M. Neumann, Q. D. Nguyen, P. A. Rosen, J. G. Shimada, M. Simard, W. W. Tung

January 2022

National Aeronautics and
Space Administration

Jet Propulsion Laboratory
California Institute of Technology
Pasadena, California

DOCUMENT CHANGE LOG

Revision	Cover Date	Notes
	January 2019	Initial release
	January 2020	Clarified file name convention, fill value, no data value, valid range, & scale factor for products. Made other minor updates.
V1.1	January 2022	Updated File Name Conventions

TABLE OF CONTENTS

1 Introduction....1
2 SRTM Mission Background....2
3 NASADEM Products....2
3.1 File Name Convention....2
4 NASADEM SRTM Radar Processing Improvements....4
4.1 Phase Unwrapping....4
4.1.1 Approach....4
4.1.2 Results....6
4.2 Height Ripple Error Correction (HREC)....8
4.2.1 Introduction....8
4.2.2 Dataset Description....9
4.2.3 Approach....13
4.2.4 GCP Characteristics as a Function of Land Cover....17
4.2.5 Example Height Ripples and Corrections....22
4.2.6 Continental Processing and Results....31
4.2.7 Conclusion....32
4.3 Height Precision Estimation....34
5 NASADEM Finishing....34
5.1 DEM Merging....34
5.1.1 Ellipsoid to Geoid Conversion....34
5.1.2 Water Masking....34
5.1.3 Unwrapping Error Detection and Removal....36
5.1.4 ASTER GDEM, ALOS PRISM AW3D30 DEM, and Void Filling....36
5.1.5 GDEM Error Mask Generation....37
5.1.6 Remaining DEM Merging Steps....41
5.2 Slope and Curvature....41
5.2.1 Input Data....41
5.2.2 Surface Fitting....41
5.2.3 Slope and Curvatures....43
6 Acknowledgments....44
7 Data Access....44
8 Contact Information....44
9 Acronyms....44
10 References....45

TABLE OF FIGURES

Figure 1. NASADEM phase unwrapping block diagram 6
Figure 2. Elevation maps showing void reduction from improved phase unwrapping using SNAPHU 7
Figure 3. SRTM InSAR antenna boom geometry 9
Figure 4. SRTM orbit passes per one-degree grid cell 10
Figure 5. ICESat GLAS shot density 12
Figure 6. HREC processing flow 13
Figure 7. HREC parameter estimation over range and along-track dimensions 15
Figure 8. Lidar elevation metrics rh100, rh50, and rh0 19
Figure 9. SRTM elevation transects compared to ICESat GLAS elevation metrics 19
Figure 10. SRTM / ICESat GLAS vegetation bias considerations 19
Figure 11. SRTM / ICESat GLAS incidence angle considerations 21
Figure 12. Example height ripples over ocean 25
Figure 13. Example height ripples over interior land 26
Figure 14. Example height ripples over a coastal region 27
Figure 15. Correction results for ocean example 28
Figure 16. Correction results for interior land example 29
Figure 17. Correction results for coastal region example 30
Figure 18. Coverage characteristic histograms for North America strip height datasets 31
Figure 19. ICESat and SRTM elevation uncertainties for North America 31
Figure 20. Histograms of average error characterisitics throughout North America processing 33
Figure 21. Histograms of HREC average offset and roll angle slope for North America 33

TABLE OF TABLES

Table 1. NASADEM products and their groupings 3
Table 2. NASADEM NUM file index associated with merged hgt file 4
Table 3. NASADEM phase unwrapping strip-level void improvement statistics 7
Table 4. Bias between SRTM phase center and ICESat GLAS elevation metrics over vegetated areas 20
Table 5. North America HREC strip dataset performance using the linear model 32

1 INTRODUCTION

NASADEM is a modernization of the Digital Elevation Model (DEM) and associated products generated from the Shuttle Radar Topography Mission (SRTM) data. We reprocessed the original SRTM raw signal radar data using improved algorithms and incorporating data primarily derived from the Ice, Cloud, and Land Elevation Satellite (ICESat) Geoscience Laser Altimeter System (GLAS) and Advanced Spaceborne Thermal Emission and Reflection Radiometer (ASTER) instruments. These lidar and DEM data were unavailable during the original SRTM processing. The NASADEM products are freely available through the Land Processes Distributed Active Archive Center (LP DAAC) at one-arcsecond spacing.

The most significant processing improvements involve void reduction through improved phase unwrapping and using ICESat GLAS data for control. The updated processing strategy now includes an alternative phase unwrapper for data processing patches where the unwrapped coverage from the original unwrapper falls below a coverage threshold. Patch boundary voids are mitigated by reprocessing with different along-track starting locations in the data and merging the unwrapping results. We also updated a low-resolution elevation database to aid with phase unwrapping bootstrapping, retaining isolated component of unwrapped phase, and assessing the quality of the strip DEMs.

We introduced a height error correction algorithm to reduce artifacts in the strip elevation data. These height ripples are a few meters in size and have along-track spatial scales of tens of kilometers. The source of the problem is uncompensated mast motion from the original data collection and is most pronounced after Shuttle roll angle adjustment maneuvers. Our along-track filtering approach utilizes differences between the SRTM heights and ICESat GLAS elevation data to correct the SRTM strip DEMs.

After merging and regridding the strip DEMs into 1x1-degree tiles, remaining voids are primarily filled with the ASTER-derived Global DEM (GDEM). We use a delta surface fill method to rubber-sheet the fill data across the void for a seamless merger. Finally, a new post-processing module creates DEM-derived products from the void-free elevation data. The slope, aspect, plan curvature, and profile curvature are found by fitting a local surface at each DEM posting and computing metrics from the fit coefficients.

This document is organized as follows: We provide a summary of the SRTM mission (Section 2) and NASADEM products (Section 3). We then provide technical details and example results from the NASADEM SRTM radar processing improvements (Section 4). We also describe the finishing processes of void filling and slope and curvature generation (Section 5). Ancillary and auxiliary input datasets and their conditioning for use in the NASADEM processing are also described in the processing improvements and finishing sections.

2 SRTM MISSION BACKGROUND

SRTM was a joint project of NASA and the National Geospatial-Intelligence Agency (NGA) that included the German and Italian space agencies as partners. The mission flew for eleven days in February 2000 on the orbiter Endeavour. The imaging objective was to use synthetic aperture radar (SAR) interferometry (InSAR) to collect sufficient data to generate digital elevation maps (DEMs) of the 80% of the global landmass that lies between ±60° latitude. The project used the Shuttle Imaging Radar-C (SIR-C) hardware that had flown twice before on the Space Shuttle, augmented with an additional radar antenna at the end of a sixty-meter mast. The radar and antennae arrangement formed a fixed-baseline ScanSAR interferometer alternatingly illuminating four subswaths (beams) (Farr et al., 2007).

SRTM was an unqualified success. The US C-band radar imaged more than 99.9% of the targeted landmass at least once, 95% at least twice, and over 50% at least three times. The additional coverage from different vantage points allowed for filling in shadowed areas and improving the vertical resolution of the resulting maps. The NGA DEM specification called for vertical errors smaller than sixteen meters absolute relative to the center of the Earth at the 90% level, with data points spaced every one arcsecond in latitude and longitude. Performance evaluations by NGA, the US Geological Survey (USGS), the SRTM project and independent investigators have shown these errors to be generally smaller than eight meters in sparsely vegetated areas (Rodriguez et al., 2006; Carabajal and Harding, 2005; Carabajal and Harding, 2006). Additional SRTM data details are provided in the height ripple error correction discussion (Section 4.2.2.1).

3 NASADEM PRODUCTS

NASADEM output products are flat binary files in big endian byte order with 3601 rows and 3601 columns. The data type and units differ by product (Table 1).

Note that the integer heights in the merged void-free DEM files are relative to the EGM96 geoid whereas the floating-point heights in the SRTM-only DEM files are relative to the WGS84 ellipsoid.

The tot_cor product is the total unbiased ramped correlation (includes volumetric, signal-to-noise ratio (SNR), and geometric correlation sources) where unbiased means the correlation estimator bias is removed. The vol_cor product is the volumetric biased deramped correlation (includes volumetric and SNR correlation sources) where deramped means the terrain interferometric fringes are removed prior to correlation estimation.

3.1 File Name Convention

The following file name convention applies to all NASADEM products (Table 1):

Example: NASADEM_HGT_n04w075.zip

NASADEM_HGT = product short name

n04w075 = southwest geographic coordinate of tile

Table 1. NASADEM products and their groupings

Product	Description	Data Type	Units	Fill Value	No Data Value	Valid Range	Scale Factor
NASADEM_HGT: NASADEM Merged DEM Product Grouping							
hgt	Void-filled DEM merge	2-byte signed integer	meters **(relative to the EGM96 geoid)**	N/A	N/A	-32767 to 32767	N/A
num	NUM file associated w/ hgt file	byte	Class: See Table 2	N/A	N/A	0 to 255	N/A
swb	Updated SRTM water body data	byte	Class: 0 for land, 255 for water	N/A	N/A	0, 255	N/A
NASADEM_SC: NASADEM Slope and Curvature Product Grouping							
slope	Slope derived from hgt	2-byte unsigned integer	hundredths of degrees (0 = water)	0	NaN	Non-negative	See Units
aspect	Slope aspect angle derived from hgt	2-byte unsigned integer	hundredths of degrees clockwise from north (0 = water)	0	NaN	Non-negative	See Units
plan (planc)	Plan curvature derived from hgt	4-byte real	inverse meters (0 = water)	0	NaN	-	N/A
profile (profc)	Profile curvature derived from hgt	4-byte real	inverse meters (0 = water)	0	NaN	-	N/A
swbd (swb)	Updated SRTM water body data	byte	Class: 0 for land, 255 for water	N/A	N/A	0, 255	N/A
NASADEM_SSP: NASADEM SRTM Subswath Product Grouping							
tot.cor	Radar total correlation	2-byte unsigned integer	correlation value * 10000 (0 = void)	0	N/A	Non-negative	See Units
vol.cor	Radar volumetric correlation	2-byte unsigned integer	correlation value * 10000 (0 = void)	0	N/A	Non-negative	See Units
img	Radar individual images	byte	DN + 128 (0 = void) (i.e., fileValue = 10 * log10(actualValue) + 128)	0	N/A	-	See Units
inc0	Radar incidence angle (relative to ellipsoid)	2-byte unsigned integer	hundredths of degrees (0 = void)	0	N/A	Non-negative	See Units
inc	Radar incidence angle (local)	2-byte unsigned integer	hundredths of degrees (0 = void)	0	N/A	Non-negative	See Units
NASADEM_SIM: NASADEM SRTM Image Mosaic Product Grouping							
img_comb (img)	Radar combined images	byte	DN + 128 (0 = void) (i.e., fileValue = 10 * log10(actualValue) + 128)	0	N/A	-	See Units
img_comb_num (img.num)	NUM file associated with combined images	byte	Number of pixels averaged for each img_comb output pixel	0	N/A	0 to 10	N/A
NASADEM_SHHP: NASADEM SRTM-only Height and Height Precision Product Grouping							
hgt_srtmOnly (hgts)	SRTM-only floating-point DEM	4-byte real	meters **(relative to the WGS84 ellipsoid)**	-32768	N/A	-	N/A
err	Height error (precision)	2-byte unsigned integer	millimeters (32769 = void)	32769	N/A	Non-negative	N/A

Table 2. NASADEM NUM file index associated with merged hgt file

Value	Description
0	Water in corrected SRTM water body data
1-23	SRTM 1-23 (max known is 23)
41-94	PRISM 1-50 (54 max polar, 37 max elsewhere)
110-160	GDEM3 (saturated at 50)
170-220	GDEM2 (saturated at 50)
231	SRTMv3 from GDEM3
232	SRTMv2 from GDEM3
233	SRTMv2 from GDEM2
234	SRTM-with-NGA-fill from GDEM2
241	NED from GDEM2 (USA)
242	NED from GDEM3 (USA)
243	CDED from GDEM2 (Canada)
244	CDED from GDEM3 (Canada)
245	Alaska from GDEM2 (Alaska)
246	Alaska from GDEM3 (Alaska)
250	Interpolation
251	Quad edge averaged where two neighboring quads disagreed (generally a GDEM error)
255	ERROR (if NUM IS MISSING - none known to exist)

4 NASADEM SRTM RADAR PROCESSING IMPROVEMENTS

4.1 Phase Unwrapping

This section describes improvements we made to the SRTM phase unwrapping approach in order to map elevation more accurately and reduce the size and occurrence of data voids.

4.1.1 Approach

The SRTM DEM was produced using a conservative, residue-based phase unwrapping algorithm (Goldstein et al., 1988) that masked large areas where the unwrapped phase solution was considered unreliable. As a result, a significant number of data voids occurred in regions with severe topography or low signal-to-noise ratio (SNR). For phase ambiguity adjustment, the previous SRTM algorithm used a 15-arcsecond low-resolution database (LRDB) created by merging several old DEM sources (primarily DTED-1 and GLOBE DEM) available prior to the SRTM mission.

As part of the NASADEM development effort, we made three major improvements to the SRTM InSAR processor to reduce the presence of voids and extend the overall DEM coverage:

- The Statistical-cost Network-flow Algorithm for Phase Unwrapping (SNAPHU) software was integrated into the SRTM processing flow as an alternative unwrapping method.
- The LRDB was upgraded with more modern, accurate and finer-resolution DEM sources.
- Several phase unwrapping solutions of the same area obtained by shifting the data processing patch boundaries are now compared and merged for quality assessment and coverage improvement to form the final DEM product.

SNAPHU computes congruent phase-unwrapped solutions that are maximally probable in an approximate a-posteriori sense (Chen and Zebker, 2001). Using statistical cost functions in conjunction with a network optimization solver, SNAPHU provides potentially better unwrapped phase solutions compared to the residue method because scattering phenomena such as layover and shadow are properly modeled in the cost functions. Our initial experiments showed that SNAPHU reduced the void area by more than 50% without reducing the DEM quality but with processing times as much as 250 times longer than the residue method.

To take advantage of SNAPHU for the entire SRTM dataset, we designed a hybrid residue/SNAPHU unwrapping strategy (Figure 1). The NASADEM processor forms single-look complex images and interferograms for each SRTM patch, and unwraps the patch interferograms using first the original residue method. SNAPHU is activated if the correlation and the coverage of the residue phase unwrapping solution are below pre-defined thresholds. The solution returned by SNAPHU is then retained if the unwrapped-phase coverage and the phase variance at the patch boundaries show improvement compared to the residue-based solution.

Phase ambiguities modulo-2π are resolved by bootstrapping the unwrapped phase between overlapping patches (when possible), and by comparing the unwrapped phase against the new LRDB. The new, higher-spatial-resolution LRBD consists of SRTM Plus (i.e., SRTM NASA Version 3) at three arcsecond spacing, with a one-additional-degree of latitude extension north to 61N. SRTM Plus includes all of the original SRTM DEM but with voids filled primarily by ASTER GDEM2 and secondarily by oversampled GMTED2010 and USGS NED, where available. The extension uses SRTM Version 1 filled and extended by GDEM2. Using a finer and more accurate LRDB helps retain isolated limited-size connected components of unwrapped phase, such as those associated with small islands, which were discarded by the previous SRTM algorithm.

In addition to using SNAPHU and the new LRDB, we also introduced a novel burst-shifting mechanism that shifts the patch boundaries within the SRTM strip processing to generate alternative phase unwrapping solutions for the same area on the ground. These solutions are compared with each other and against the LRDB in order to detect and mask possible unwrapping errors, and ultimately merged to form a single, improved elevation map.

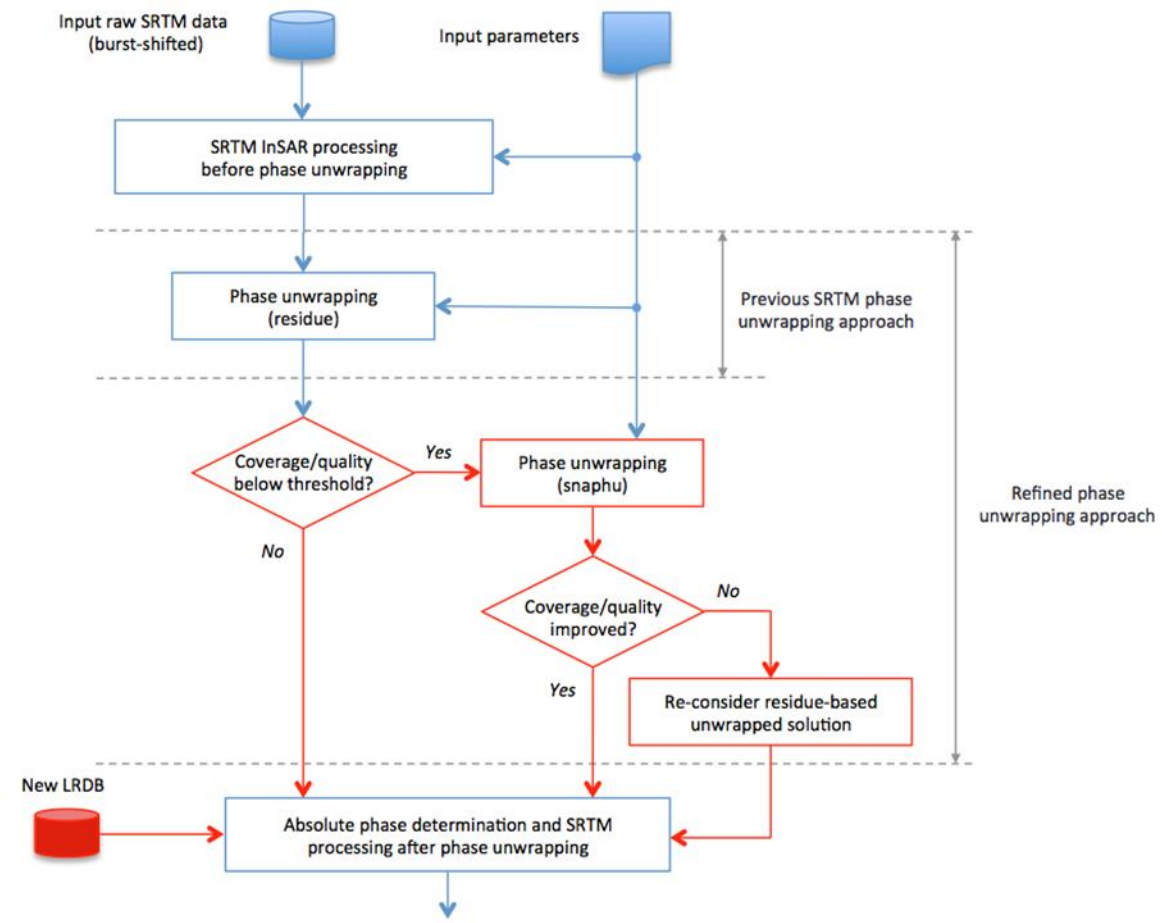

Figure 1. NASADEM phase unwrapping block diagram

4.1.2 Results

The phase unwrapping strategy was tested with several SRTM strips acquired in areas with large presence of voids. Elevation maps over steep terrain show void reduction when comparing the NASADEM SNAPHU phase unwrapping to the original SRTM residue-based phase unwrapping (Figure 2). The image is located in the Andes Mountains at (2.5 degrees North latitude, 78.69982485 degrees West longitude) with blue areas representing voids. The large voids correspond to areas masked by the residue algorithm (Figure 2(a)). These voids appear to be significantly reduced in number and size after applying SNAPHU (Figure 2(b)). In addition, the new phase unwrapping strategy mitigates the occurrence of sharp boundaries between adjacent patches. In this particular example, all pixels successfully unwrapped by the residue method were successfully unwrapped by SNAPHU with an RMS difference of ~0.001 m. Patch boundary phase variance was found to be smaller for the new unwrapping, supporting the validity of our approach.

Global coverage improved significantly in regions with severe topography whereas improved only marginally over desert regions where the SAR signal-to-noise ratio is typically low. Overall, more than 50% of the void areas in the original strip data results were successfully unwrapped using SNAPHU and the multi-burst approach (Table 3).

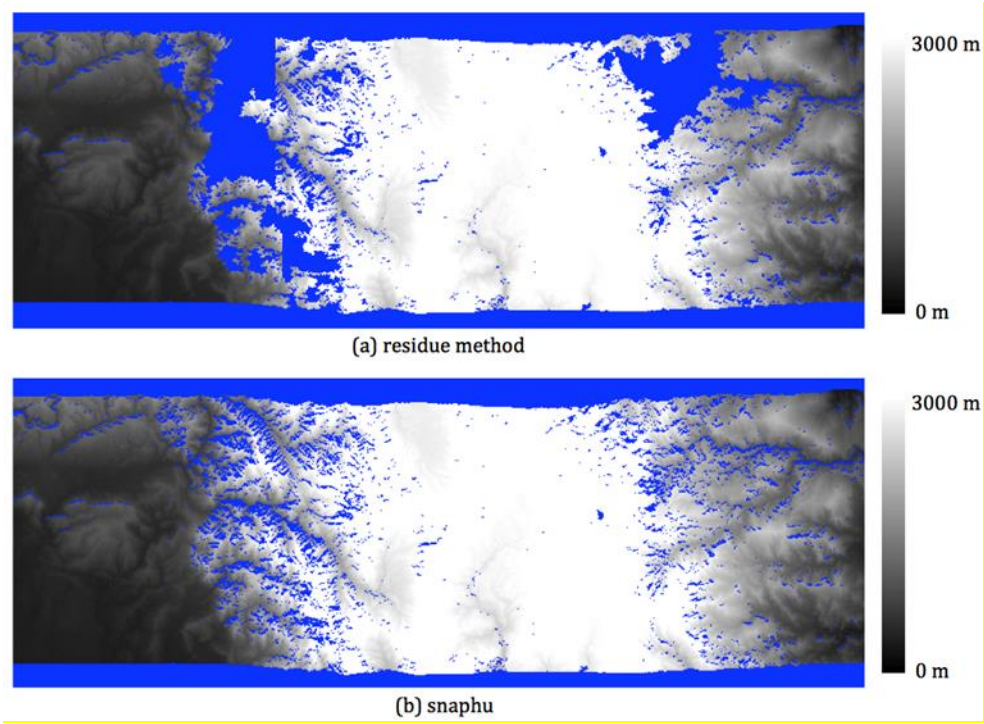

Figure 2. Elevation maps showing void reduction from improved phase unwrapping using SNAPHU

Table 3. NASADEM phase unwrapping strip-level void improvement statistics

Continent	Sample Size (# 10^9 pixels)	% Coverage at Strip Level		% SRTM Voids Now Filled…	
		SRTM	NASADEM	Using SNAPHU Unwrapper	+ Using Multi-Burst Approach
North America	155.76	95.16	97.67	34.29	51.87
South America	48.22	92.78	96.64	37.91	53.47
Eurasia	295.83	94.70	97.47	32.99	52.28
Africa	23.71	93.48	97.58	46.76	62.94
Australia	120.55	90.41	95.92	40.85	57.48
How Computed	T	$\frac{T - V_S}{T}$	$\frac{T - V_{N2}}{T}$	$\frac{V_S - V_{N1}}{V_S}$	$\frac{V_S - V_{N2}}{V_S}$

T : Total number of strip samples processed

V_S : Number of strip void samples in original SRTM, including land and water

V_{N1} : Number of strip void samples in NASADEM before multi-burst merging, including land and water

V_{N2} : Number of strip void samples in NASADEM after multi-burst merging, including land and water

4.2 Height Ripple Error Correction (HREC)

This section describes a new approach to mitigate SRTM DEM height ripples introduced by uncompensated shuttle boom motion and other systematic height errors. The adaptive correction of the ripples uses available lidar data from ICESat GLAS over land, and modeled ocean surface topography over coastal regions. We present continent-scale results for North America.

4.2.1 Introduction

SRTM produced an unprecedented near-global DEM of the world Farr et al. (2007). Since its release, the SRTM DEM is widely used in many research, commercial, and military applications. Its accuracy has been independently evaluated over various regions of the world and found to be better than the original mission specifications (e.g. Carabajal & Harding (2005); Bhang et al. (2007)).

The objective of the NASADEM project is to improve the SRTM DEM height accuracy and data coverage, and provide additional SRTM radar-related products. The improvements are achieved by reprocessing the original SRTM radar echoes and telemetry data with updated algorithms and auxiliary data not available at the time of the original SRTM production. After SRTM flew, several missions acquired surface topography information, most notably the ICESat GLAS instrument (Zwally et al., 2002) and the TanDEM-X mission (Krieger et al., 2007; Gonzalez et al., 2010). However, the ICESat GLAS satellite lidar instrument provides only sparse point measurements of surface elevations, though with high accuracy. On the other hand, the TanDEM-X mission provides comprehensive coverage but as a public-private partnership, its highest resolution DEM is not freely available.

One known issue of the SRTM DEM is the observed height ripples caused by uncompensated SRTM antenna boom motion (Gallant & Read, 2009). The imprecise knowledge of the true interferometric orientation angle, on the order of a few arcseconds or a millimeter of baseline positioning, results in elevation errors up to a few meters.

We present here an approach to compensate for these elevation ripples based on a high-resolution correction of strip data in radar geometry prior to mosaicking and regridding that is derived from a dense distribution of ground control points (GCPs). These GCPs come from elevation estimates from ICESat GLAS) over land (Zwally et al., 2002), and from the modeled ocean elevation topography over the ocean (Rodriguez et al., 2005). Forest areas are handled separately from bare ground surfaces because of the limited SRTM microwave penetration within the forest canopy. In these areas, the SRTM C-band phase center height inside the canopy is estimated using ICESat GLAS waveforms (Carabajal & Harding, 2006; Simard et al., 2011). While the height ripple error correction (HREC) module was originally intended to correct uncompensated boom motion effects due to the firing of the shuttle thrusters, our approach also compensates for other systematic errors observed in the strip data.

The HREC section is organized as follows. Section 4.2.2 presents the characteristics of the data sets: SRTM, ICESat, and ocean topography data. Section 4.2.3 outlines the processing methodology with description of the individual algorithms, including data transformations, error and uncertainty estimations, weighted least-squares estimation of the range-function model parameters, and the polynomial moving average operation in the along-track dimension. Section 4.2.4 discusses the land cover specific adjustments in the error correction. In particular, the effect

of potential changes between SRTM and GCP data acquisition is discussed, as well as the nuances and compensation of effects caused by vegetation, ice/snow, and sloped terrains. Section 4.2.5 demonstrates the observed errors and the performed correction on a few example datasets, covering ocean, sloped terrain, vegetation, and at areas. Performance results using SRTM data over the North American continent are presented in Section 4.2.6. Finally, Section 4.2.7 concludes the discussion.

4.2.2 Dataset Description

This section summarizes the main data sources used in the HREC module, namely the SRTM and the ICESat lidar data, the modeled ocean surface elevations, and the land-water mask used to distinguish land from the ocean.

4.2.2.1 SRTM

SRTM provided a near-global topographic map of the world (Figure 3, Farr et al. (2007)). It used single-pass Synthetic Aperture Radar Interferometry (InSAR) (Bamler & Hartl, 1998; Rosen et al., 2000) to generate DEMs of 80% of the landmass between -56 and 60 degrees latitude (Figure 4). The data acquisition took place in February 2000, when the SRTM instrument flew for eleven days on the space shuttle orbiter Endeavour. The data was acquired at C-band frequency (5.6 cm wavelength) in four-beam ScanSAR mode, with the effective ground resolution varying between 45 and 60 m (Smith & Sandwell, 2003). The InSAR instrument, with a 60-m separation between the two radar antennae, provided height ambiguities along the swath from 125 to 325 m.

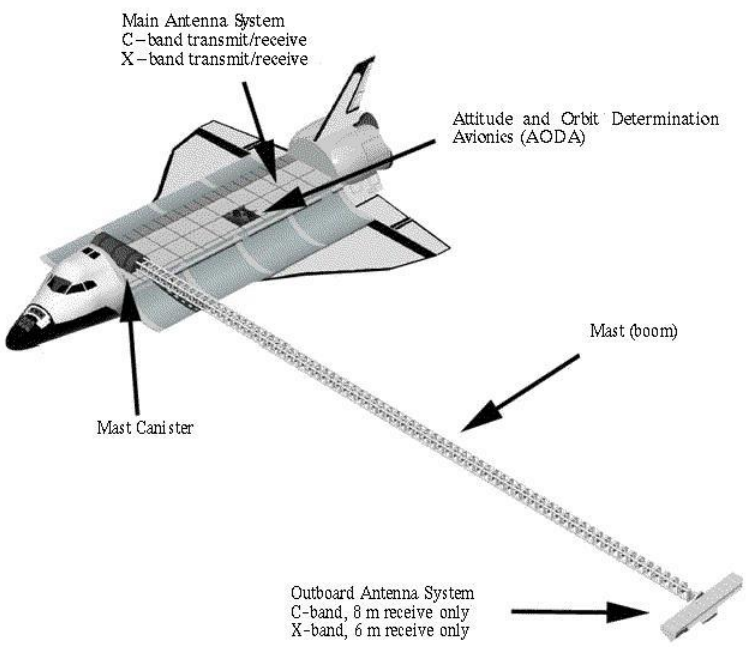

Figure 3. SRTM InSAR antenna boom geometry

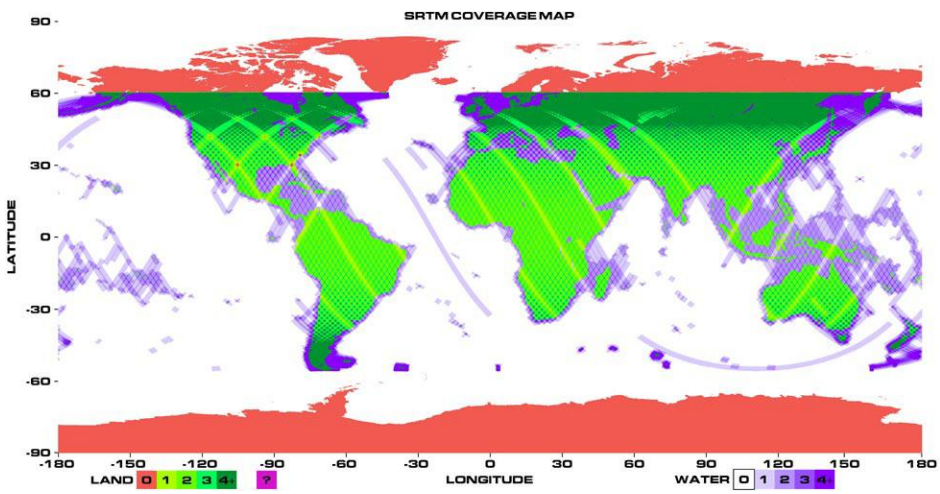

Figure 4. SRTM orbit passes per one-degree grid cell

The mission performance requirements at the 30-m spatial resolution consisted of 16-m absolute vertical error, 10-m relative height error, 20-m absolute lateral geolocation error, and 15-m relative geolocation error (90% errors). The performance does vary spatially and is dependent on the land cover type. A global assessment of the SRTM performance showed the average absolute and relative height errors to be ~6.8 m and 7 m, respectively, and the absolute geolocation error to be ~9.7 m (Rodriguez et al., 2005, 2006). These estimates were verified by other independent studies over smaller local areas (e.g. Carabajal & Harding (2005); Bhang et al. (2007)).

SRTM InSAR error sources can be divided into static and dynamic errors, and are described in detail in Rodriguez et al. (2006). Static errors are time-invariant and can be compensated by means of targets with known global locations. Time-varying errors are due to uncompensated motion of the interferometric baseline and changes in the interferometric phase due to changes in electronic beam steering. These error sources include (1) phase errors due to random thermal and geometric decorrelation noise due to systematic antenna pattern mismatches or long term drift of the instrument electronics; (2) baseline roll errors due to imprecise knowledge of the baseline roll angle, (3) differential errors at the beam overlaps; and (4) timing and position errors due to uncompensated timing delays or antenna position estimation inaccuracies.

The original vertical height error budget allocated 9 m to random and systematic phase noise, 8 m to baseline roll angle inaccuracy, and 3 m to all other error sources including platform location, baseline length and range distance inaccuracies. Of most importance for HREC are the uncompensated baseline estimation errors caused by the limited knowledge of the baseline roll angle. These errors lead to cross-track slope errors in the estimated topography whose magnitude is equal to the roll error. The height error δ_h is proportional to the ground range distance x and the baseline roll angle error δ_a:

$$\delta_h = x\delta_a \tag{1}$$

Given the nominal shuttle altitude of 233 km and look angles ranging from 30 to 60 degrees, a roll angle knowledge better than 0.14 millidegrees is required to keep the height error to less than 1 meter, or equivalently a slope error of approximately 2 mm per 1 km ground distance.

The Attitude and Orbit Determination Avionics (AODA) metrology system was used to estimate the baseline position. The main components of the baseline motion are due to the natural modes of oscillation of the SRTM antenna mast excited by thruster firing that are used to maintain the baseline orientation that occurred every ~8 seconds or ~60 km along the orbit. The time scale for other residual roll errors is long, resulting in spatial errors with wavelengths on the order of thousands of kilometers. They constitute the primary source for long-wavelength residual errors.

The original error compensation strategy of SRTM consists of three parts: (1) along-track calibration to estimate beam to beam discontinuities; (2) dynamic calibration to estimate static phase screens (Hensley et al., 2001) and time changing residual phase and roll errors (based on long wavelength ocean topography); and (3) mosaicking and assimilating multiple datasets together, using available GCPs and pass-to-pass tie points.

Since the boom motion errors are orbit dependent, the height ripple error correction (HREC) is performed on individual orbit strips (called peg regions) in the radar geometry, whose axes are the range (cross-track) and along-track and the across-track directions. The individual strip dimensions, combining the four SRTM beams together (Farr et al., 2007), are approximately 225 km across-track and over 1,000 km along-track. The height error correction is performed on the data with a 30-meter resolution. The random error SRTM height uncertainties are derived from the interferometric coherence (Rosen et al., 2000).

4.2.2.2 ICESat GLAS

ICESat was launched January 12, 2003 from Vandenberg Air Force Base in California into a near-circular, near-polar, 600 km altitude orbit. The ICESat mission was designed to provide elevation data needed to determine ice sheet mass balance as well as cloud property information, especially for stratospheric clouds common over polar areas. However, ICESat also provided an unprecedented dataset of surface elevation and forest canopy measurements around the globe (Figure 5). The sole instrument on ICESat is GLAS, a space-based lidar. GLAS combines a precision surface lidar with a sensitive dual-wavelength cloud and aerosol lidar. The GLAS lasers emit infrared and visible laser pulses at 532 and 1064 nm wavelengths, the latter being used for the land surface altimetry products (called GLA14). The data is referenced to the TOPEX/Poseidon ellipsoid. The laser has a footprint of about 65 m and elevation measurements are separated by nearly 172 m along the spacecraft ground track. The equatorial cross-track spacing is tens of kilometers and depends on cloud coverage. The elevation accuracy over at bare ground is sub-decimeter but can be significantly larger over sloped terrain (Fricker et al., 2005). Moreover, GLAS can also be used to estimate canopy height as presented, for example, in Simard et al. (2011); Lefsky (2010) and ground elevation below the canopy as shown in Neuenschwander et al. (2008).

For the current demonstration of NASADEM error correction, the latest version of GLAS land product GLA14 (currently V6.34) was used. Numerous criteria were used to select GLAS shots and to assess the quality of the elevation measurements for both bare ground and forested shots (Simard et al., 2011). A common set of criteria were derived based on the SNR, elevation realism, and saturation. We only selected the waveforms with SNR greater than 50. This criterion

was found to remove most faulty elevation measurements. In addition, to remove ICESat shots potentially rejected from clouds, we rejected all shots with elevation difference greater than 80 m with respect to the original SRTM product.

Bare ground and forest shots were distinguished using the number of detected peaks. Any shots with lidar waveforms exhibiting more than one observed peak were identified as forested landscape while waveforms with single peaks were identified as bare ground shots. The waveform centroids were computed for bare ground shots to estimate ground elevation. In the case of forested shots, the last returned peak was used to locate the ground below canopy. We used the width of the ground peak as an estimate of elevation measurement uncertainty.

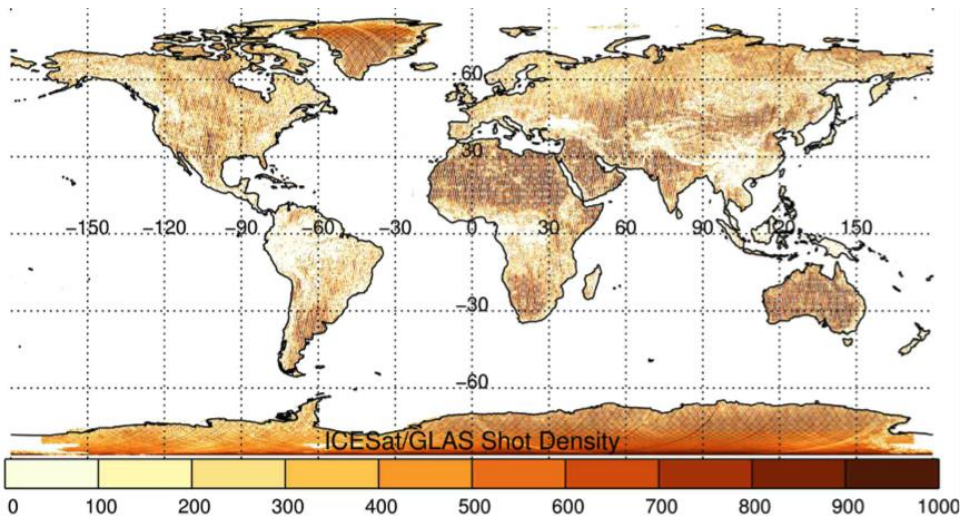

Figure 5. ICESat GLAS shot density

4.2.2.3 Ocean Topography

The ocean surface topography is computed based on the geoid, the ocean circulation, and tidal changes. The errors in the topography are assumed much smaller than 50 cm (Rodriguez et al., 2005). For the SRTM mission, the EGM96 geoid, the TOPEX mean sea surface together with a tidal model tuned for coastal accuracy were used to generate ocean ground-truth surfaces (Tierney et al., 2000).

For the HREC, ocean surface elevations are transformed to the SRTM radar geometry coordinates of the individual SRTM strip beams, and GCPs are generated with a spatial separation of 500 m. An upper limit for the ocean GCPs uncertainty of 0.5 m was assigned.

4.2.2.4 Land-Water Mask

In order to distinguish land from ocean and other water bodies for the selection of ICESat and ocean elevation GCPs, the SRTM water body datasets (SWBD) were used. SWBD data are a by-product of the SRTM data editing performed by the National Geospatial-Intelligence Agency (NGA, 2003) to produce the finished SRTM Digital Terrain Elevation Data Level 2. Ocean, lake and river shorelines were identified and delineated.

The SWDB vector files are rasterized and the content transformed to SRTM radar geometry coordinate system for the individual beams. For every SRTM strip data set, the land-water mask classifies the most likely land cover type, distinguishing four categories: land, ocean, lake, and river.

4.2.3 Approach

This section presents the error correction approach and algorithms. The HREC processing flow consists of three stages (Figure 6). The first stage includes data preprocessing, transformations and GCP selection. In the second stage, the errors and uncertainties are computed and the error correction parameters are estimated at the level of the point clouds. In the third stage, the elevation corrections are applied on the individual SRTM beam strips. A strip is a portion of data acquired in a pre-selected orbit leg. The length of a strip varies with latitude and decreases from 10 degrees in latitude at equator to less than two degrees at the North and South borders of SRTM data coverage (around 60 degrees). Every strip consists of four sub-swaths corresponding to the four ScanSAR beams designed to cover the 225 km swath. The beams are characterized by a range of incidence angle and polarization configurations (i.e., HH or VV). All beams are impacted by acquisition geometry and other systematic errors, and the corrections factors are therefore estimated considering all four beams simultaneously.

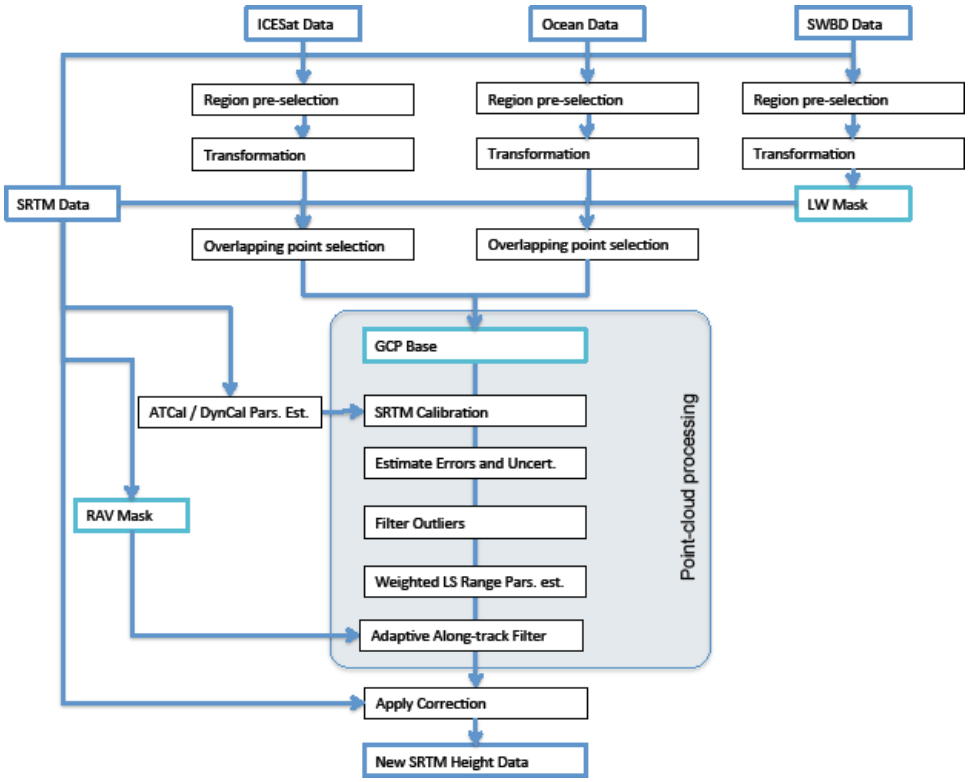

Figure 6. HREC processing flow

4.2.3.1 GCP Data Preparation

ICESat GLAS data are separated into bare ground and vegetation datasets, as described in Section 4.2.2.2. Over vegetated areas, the lidar waveform profile is reconstructed in order to enable the reference height selection between rh0 (ground) and rh100 (canopy top). The SRTM phase center elevation is between GLAS metrics rh40 and rh75. These metrics represent relative height (RH) percentile containing a percentage of the reflected waveform energy. Uncertainties are computed based on the spread of the lidar waveform that accounts for the increased uncertainty of the location of the SRTM phase center. The ICESat elevations are referenced to the TOPEX/Poseidon datum and given as ellipsoid heights. The SRTM elevations are referenced to the WGS84 ellipsoid. Therefore, the ICESat heights need to be transformed by removing the offset between the WGS84 and the TOPEX/Poseidon ellipsoids (Bhang et al., 2007; Meyer, 2010). The correction is a function of latitude and is about 70 cm in average.

Following the computation of the ocean topography elevations and land-water masks as described in Section 4.2.2.3 and Section 4.2.2.4, the ICESat, ocean elevation, and land-water mask data are transformed from the geodetic coordinate system to the SRTM radar geometry.

The result is a point cloud database with valid SRTM and GCP elevation values. Every elevation value h_{GCP} has an associated uncertainty, or variance, σ^2_{GCP}. For the remaining of Section 4.2, no distinction is made between the GCP points due to their source of origin.

4.2.3.2 Errors and Uncertainties

The SRTM sub-swaths are usually overlapping with height measurements from different beams and with different height error characteristics. In order to obtain the best minimal variance height estimate, a variance weighted average of the heights from the two neighboring beams. Given two height measurements over the same pixel in two adjacent sub-swaths b_i, b_j, the weighted height average and variance for the pixel are:

$$h_{SRTM} = c_i h_{SRTM,b_i} + c_j h_{SRTM,b_j} \tag{2}$$

$$\sigma^2_{SRTM} = c_i^2 \sigma^2_{SRTM,b_i} + c_j^2 \sigma^2_{SRTM,b_j} = \frac{\sigma^2_{SRTM,b_i} \sigma^2_{SRTM,b_j}}{\sigma^2_{SRTM,b_i} + \sigma^2_{SRTM,b_j}} \tag{3}$$

where

$$c_i = \frac{1/\sigma_i^2}{1/\sigma_i^2 + 1/\sigma_j^2} = \frac{\sigma_j^2}{\sigma_i^2 + \sigma_j^2}.$$

The errors and uncertainties of overlapping SRTM and GCP heights are then given by

$$y = h_{SRTM} - h_{GCP} \quad , \quad \sigma^2 = \sigma^2_{SRTM} + \sigma^2_{GCP} \tag{4}$$

where y is the error between SRTM and GCP elevation heights, and σ^2 is its variance (i.e., uncertainty).

As an additional step, we remove outliers from the computed error points. The cause for outliers can be due to significant changes between the acquisition times of both datasets, or due to unforeseen phase unwrapping errors in the SRTM data, or due to processing errors in ICESat data. A conservative threshold value of 30 m is currently used for the maximal allowed error. Note that the expected height errors due to the uncompensated boom motion are on meter scale, reaching up to 10 meters.

4.2.3.3 Range-Weighted Least Squares Estimation

The estimation of the two-dimensional correction function is split into two one-dimensional problems due to the orthogonality of the error signature in the across-track (range) and along-track dimensions (Figure 7). First, local weighted least squares estimation of an error model is performed in the range direction. The model parameters are estimated in a local 1-km-wide along-track estimation window combining GCPs over the entire swath from all 4 beams, thus using all available GCPs in the area of about 225 sq km. The processing in the along-track direction is presented in the following Section 4.2.3.5.

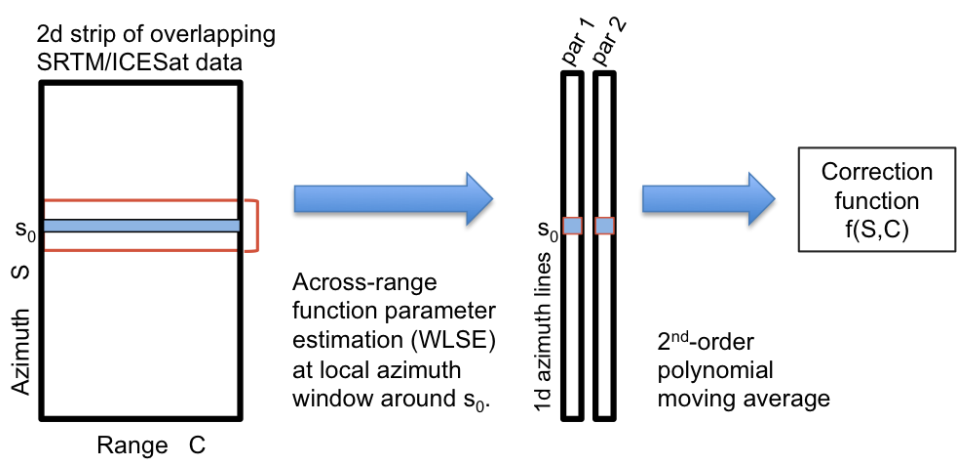

Figure 7. HREC parameter estimation over range and along-track dimensions

Imprecise knowledge of the baseline roll angle induces an error in the estimated SRTM heights that is proportional to the ground range distance and the error in baseline roll angle, as shown in Equation 1. This leads to a slope error model:

$$y = a_1 x \tag{5}$$

where y is the observed error, x is the ground range distance, and a_1 is the error slope, corresponding to the error in the baseline roll angle estimation.

To find the range slope parameter over a local along-track region the weighted least squares (WLS) method is used, minimizing the sum of weighted squares of the residuals, leading to a simple solution

$$\hat{a}_1 = \frac{\mathbf{x}^{\mathbf{T}}\mathbf{W}\mathbf{y}}{\mathbf{x}^{\mathbf{T}}\mathbf{W}\mathbf{x}} \tag{6}$$

where $\mathbf{x}$ is the vector of ground range distances, $\mathbf{y}$ is the vector of height errors, $\mathbf{W} = \mathrm{diag}(\mathbf{w})$ is the diagonal matrix of weights vector $\mathbf{w}$ (reciprocal of error uncertainty: $\mathbf{w}_i = \sigma_i^{-2}$).

However, while the slope model (Equation 5) was sufficient to correct for the errors caused by the uncompensated shuttle boom motion during thrusters firing maneuvers, it was insufficient to correct for other observed systematic error sources. Therefore, multiple polynomial models are implemented and are available in the HREC processing chain for selection. After evaluations, a simple first-order model proved to be most efficient and sufficient to correct for all observed systematic errors. Therefore, in addition to the physically motivated model (Equation 5), we examined two other simple models. First, the constant height offset model independent of range is given by:

$$y = a_0 \tag{7}$$

with the WLS solution of

$$\hat{a}_0 = \frac{\mathbf{w}^{\mathbf{T}}\mathbf{y}}{\mathbf{1}^{\mathbf{T}}\mathbf{w}} \tag{8}$$

where $\mathbf{1}$ is a vector of ones.

The linear model is then given by

$$y = b_0 + b_1 x \tag{9}$$

with the solution

$$\begin{bmatrix} \hat{b}_0 \\ \hat{b}_1 \end{bmatrix} = \left(\mathbf{X}^{\mathbf{T}}\mathbf{W}\mathbf{X}\right)^{-1}\mathbf{X}^{\mathbf{T}}\mathbf{W}\mathbf{Y} \tag{10}$$

where matrix $\mathbf{X} = \begin{bmatrix} 1 & \mathbf{x} \end{bmatrix}$ is constructed for convenience from $\mathbf{x}$. The symbols ^{T} and $^{-1}$ denote the transpose and the matrix inverse operations, respectively.

4.2.3.4 Roll Angle Variability (RAV) Mask

Under the assumption that the systematic errors are due to imprecise knowledge of baseline roll angle, a roll angle variability (RAV) mask is computed based on the telemetry data. This mask is meant to filter the occurrence of shuttle attitude maneuvers that caused significant oscillations of the outboard antenna mast. Decreasing the size of the spatial filtering window over areas with less roll variability reduces the risk of overfitting the correction function. In the current configuration, the RAV masked high-resolution areas are filtered with 6 km window sizes in along-track direction, while the low-resolution areas are filtered with up to 50 km window sizes. These window sizes were selected based on manual error inspection and the characteristic error wavelengths of shuttle boom motion induced resonances.

4.2.3.5 Along-Track Moving Average Filter

To ensure the maximum amount of spatial consistency, an along-track second-order moving average (MA) Savitzky-Golay MA (Savitzky & Golay, 1964) filter is applied to the estimated range function parameters. The second-order MA is a compromise to guarantee the adaptation to potential ripples in the data, and at the same time to avoid potential over-fitting with higher-order filters.

The along-track window size for the MA filter is adaptive depending on the roll angle variability. It usually varies between 6 km over areas with potentially strong shuttle boom motion and 30 to 50 km over areas with excellent baseline knowledge and boom motion stability.

Feathering of range parameters is performed at the intersections of the high- and low-resolution regions, as well as over extended regions with insufficient number of GCPs.

4.2.4 GCP Characteristics as a Function of Land Cover

This section presents an evaluation of SRTM and GCP height differences as a function of land cover and discusses the implications for HREC. In particular, error mitigation over vegetated, snow and ice covered, and coastal and mountainous terrains are discussed with respect to potentially introducing phase center bias and temporal changes.

4.2.4.1 Vegetated Areas

Vegetation cover decreases the accuracy of SRTM ground height estimates in two ways. On the one hand, the intrinsic InSAR volumetric decorrelation due to the vertical distribution of scatterers increases the phase noise and therefore increases the random error in the height estimate of SRTM data. On the other hand, vegetation introduces a height bias to the InSAR derived phase center height that depends on the radar frequency, polarization, incidence angle, and the vegetation cover type. The vegetation cover type effects the microwave penetration depth as a function of density, vertical distribution of vegetation particles, dielectric properties of the canopy and the ground, and the amount of surface direct and surface-vegetation double-bounce scattering contributions (e.g., Neumann et al. (2010)). This complicates the estimation of systematic SRTM height errors since the bias and the bias uncertainty are usually higher than the expected systematic SRTM height errors.

We performed an initial assessment of ICESat lidar GCPs over bare ground and vegetation. The evaluation over the challenging Amazon tropical forest area near Manaus used 32 SRTM strip beams with a total area of over seven million sq km. We found that the density of ICESat lidar shots without the vegetation bias is very low (less than one lidar bare ground GCP per fifty sq km) and usually clustered around riverbanks and human-built areas, deeming HREC unfeasible in these areas. However, when the vegetated ICESat data were included in the GCP database, the density of ICESat GCPs increased to about one GCP per two sq km. After this experiment, we elected to include ICESat data over vegetation, since otherwise the density of GCPs would be insufficient over many forests in the world.

In order to minimize the vegetation bias variability, the most consistent lidar elevation metric was selected that is both closest to the SRTM C-band phase center and least sensitive to forest height. It is observed that the ICESat GLAS waveform metric that corresponded to the measured SRTM elevation to be closest to rh50, i.e., the elevation at which 50% of the backscattered waveform energy is located (Figure 8). Note that rh100 represents the highest point of waveform power above the noise level and rh0 represents the lowest (i.e., ground) height above noise. This can be seen in an example 700-km transect over one sample strip dataset in the tropical forest (Figure 9). Next to the SRTM phase center height (red), the image shows the different ICESat elevation metrics including ground under the canopy (black), rh50 (blue), and the top of the canopy (rh100). A global distribution of SRTM bias with respect to various ICESat metrics over 349 vegetated areas (Figure 10(a)) and the corresponding statistics (Table 4) show that the ICESat rh50 metric is closest to the SRTM phase center.

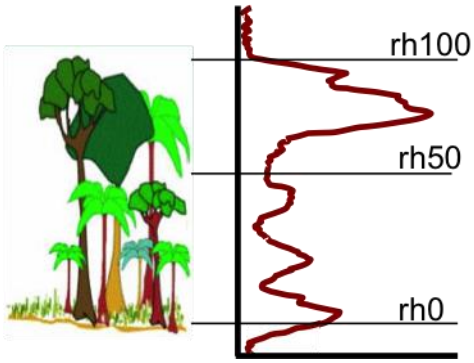

Figure 8. Lidar elevation metrics rh100, rh50, and rh0

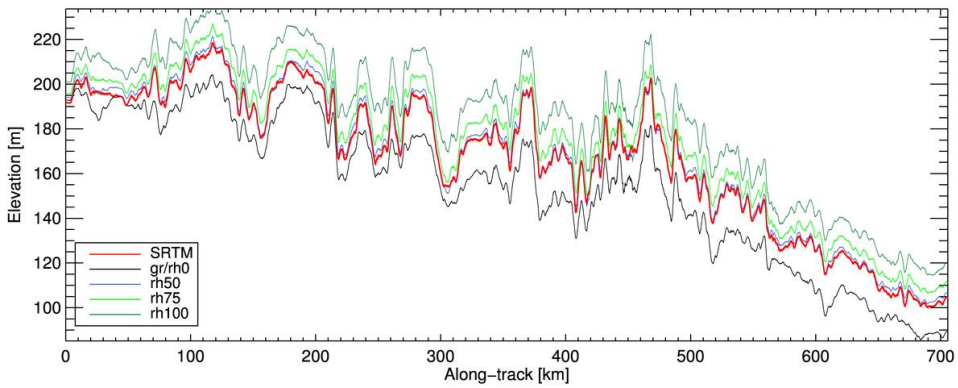

Figure 9. SRTM elevation transects compared to ICESat GLAS elevation metrics

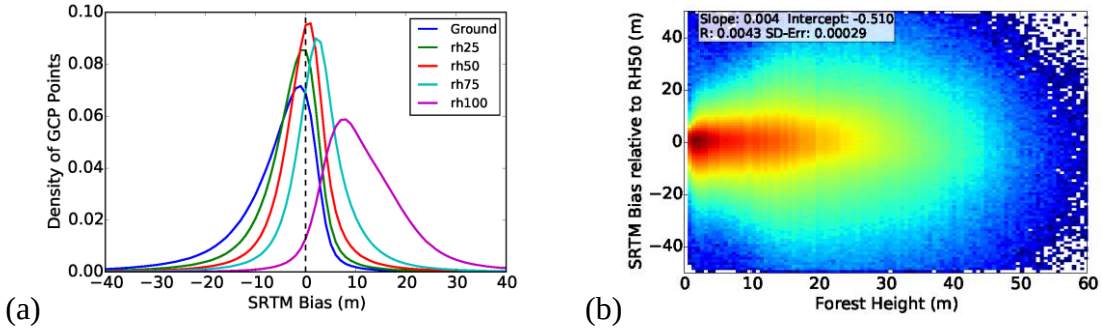

Figure 10. SRTM / ICESat GLAS vegetation bias considerations
(a) Density of vegetation bias in SRTM data with respect to ICESat GLAS height metrics. (b) SRTM / ICESat GLAS rh50 bias correlation with forest height.

Table 4. Bias between SRTM phase center and ICESat GLAS elevation metrics over vegetated areas

Lidar Metric	Mean Bias (m)	Std. Dev. (m)
rh0	-6.28	9.6
rh25	-3.38	7.9
rh40	-1.64	7.4
rh50	-0.48	7.3
rh60	0.86	7.3
rh75	2.87	7.6
rh100	11.94	9.6

Note that rh50 does not mean half of the forest height. It corresponds to the elevation in the canopy with the median scattered energy. As it depends on the density of the canopy, this can be closer to the top for dense vegetation, or closer to the ground for sparse vegetation cover. Although not a simple one-to-one relationship, a similar trend applies to radar observations of the vegetation canopy.

We evaluated whether there is a dependency of the difference between SRTM vegetation bias and ICESat GLAS rh50 elevation metric to forest height itself (Figure 10b)). As one can observe, the distribution of the rh50 minus SRTM heights over the forest height over all vegetated shots in North America is nearly independent of forest height, which was not the case for other lidar metrics. We estimate a bias over forest height slope of 0.004 m/m with a standard error of 0.0003 m/m. Consequently, we expect the forest height dependence would usually have a biasing effect of less than 10 cm and is therefore negligible when estimating ripple corrections using the rh50 metric.

We also investigated radar incidence angle-related vegetation biases. The incidence angle significantly affects the penetration depth of the electromagnetic radar waves and thus the introduced vegetation bias. In case of a homogeneous constant random volume, the vegetation bias varies in a nonlinear fashion with the incidence angle. In addition, the volumetric decorrelation noise, caused by three-dimensional distribution of scattering elements in the vegetation, is highly dependent on the incidence angle as well. In our case, the vegetation is heterogeneous in lateral and vertical directions. Therefore, an empirical relationship was derived to compensate for the incidence angle dependence on the errors. For example, for the analysis of North American data, over 63 million samples were used in the estimation that might relate to the same GCP but multiple different SRTM observations from different beams and orbits. As expected, a significant correlation was observed (Figure 11(c)), with a slope of about 70 cm height bias increase per ten degrees incidence angle change.

The uncertainties of vegetated ICESat lidar data computed for HREC represent the increased uncertainty of the location of the SRTM phase center height by increased lidar waveform spread. At the same time, the increased phase noise of SRTM data due to volumetric decorrelation increases the SRTM height uncertainty as well. The total magnified uncertainty (Equation 4) of vegetated height differences naturally reduces the weights of vegetated GCPs in the weighted least squares estimation.

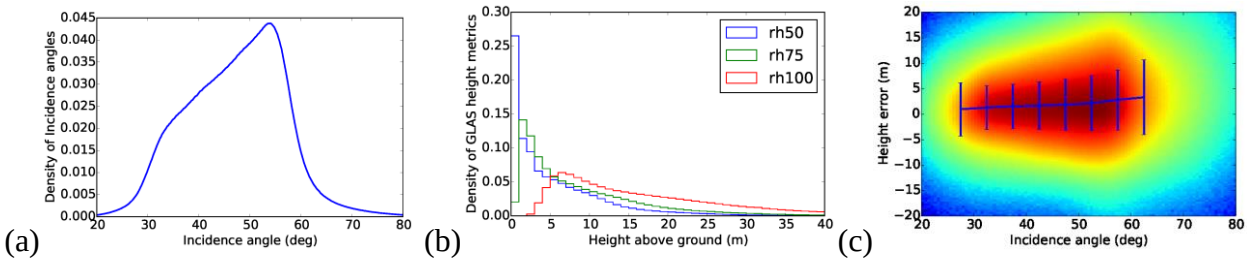

Figure 11. SRTM / ICESat GLAS incidence angle considerations
(a) Density of SRTM incidence angles. (b) Density of GLAS height metrics. (c) Density of height error over incidence angle along with the incidence angle dependent means and standard deviations of the errors.

4.2.4.2 Non-Flat Terrain

Non-flat terrain elevations have increased associated uncertainties in both SRTM and ICESat GLAS data. Similar to vegetated areas, the distribution of elevations inside the lidar footprint leads to a wider waveform. In radar data, the uncompensated parts of terrain elevations lead to increased phase noise and therefore to increased elevation uncertainty as well. The effects of non-flat terrain and volumetric scattering, such as from vegetation and snow/ice, are cumulative, so that naturally rough sloped terrain will have the largest uncertainties of elevation estimates. In addition, observing the same vegetated point over a slope from different orbits might lead to different elevation estimates due to distinctive vegetation bias.

4.2.4.3 Snow- and Ice-Covered Areas

Snow and ice cover a significant part of the SRTM imaged areas, particularly in the northern latitudes and southern latitude mountains. Not all ICESat GCPs have the same amount of snow and ice cover present at the time of acquisition as SRTM due to seasonal differences. Snow depth is generally less than the 1-2 meters that the SRTM C-band pulses penetrated (Rignot et al., 2001). On the other hand, thick glaciers significantly impact elevation measurements throughout the year, and most importantly, the significant melt of glaciers between SRTM (2000) and ICESat (2003-2009) may result in large differences in the measured heights (Sauber et al., 2005). For example, we found differences of 5-30 meters over the Malaspina Glacier in Alaska.

We adopted a GCP culling strategy to avoid the biasing effects of snow- and ice-covered lidar shots used for HREC processing. We used the MODIS-Terra snow cover products MOD10CM to identify regions potentially covered by snow during the northern (March) and southern (August) winters. We generated two composite snow cover images using all MOD10CM between 2003 and 2009. The first one represents maximum snow cover extent for the month of March and the second for August. In northern latitudes, we only use ICESat GCPs acquired during the months from May through October, which provide sufficient point density. In the southern hemisphere, we only use February-March ICESat GCPs over snow-covered areas.

To avoid height differences between SRTM and ICESat due to glacier melting, we used the Randolf Glacier Inventory (Arendt et al., 2015) to mask out all lidar shots over glaciers. The resulting global GCP dataset used to remove biases between SRTM and ICESat is representative of the ground elevation and does not affect the relative elevation of glaciers. However, height

ripples over glaciers may be relatively uncorrected in the NASADEM product since glacier GCPs are not included in the HREC processing.

4.2.4.4 GCP Summary

While there are multiple reasons that GCP heights might rightfully differ from the SRTM heights, thus complicating the systematic error correction, we addressed the main sources of differences. Since vegetated areas cover a large part of the globe, we extensively analyzed the vegetation bias effects and introduced corrections dependent on the lidar waveform metric, forest height, and incidence angle. For snow- and ice-covered areas, we preferred to limit height adjustments due to the limited amount of precise knowledge, though in most snow- and ice-covered areas one could assume that the induced height bias from the ground is less than one meter. Our best topographic knowledge originates over bare surfaces, and especially over ocean, where we have arbitrary dense spatial GCP distribution at precisely the SRTM acquisition time. While localized errors in GCPs and SRTM heights are unavoidable, the large areas over which the correction function parameters are estimated and the large quantities of GCPs support the notion that any significant errors will be reduced through averaging. Over a low-resolution 50 km along-track window, the one or two correction parameters are estimated in average using more than 11,000 land GCPs over an area of more than 11,000 sq km. In a high-resolution 6 km along-track window in areas around potential ripples, the number of land GCPs is still over 1300, on average, over more than 1,000 sq km.

4.2.5 Example Height Ripples and Corrections

This section provides examples of height ripples and other systematic errors in SRTM strip data and their subsequent correction. We examine three sample datasets that show different characteristics of the HREC processing: ocean, interior land, and a coastal region. In the following strip data figures, the four SRTM subswaths are mosaicked in range radar coordinates with the origin and orientation given by the peg point and the peg heading (Farr et al., 2007). The along-track and range coordinates are given relative to the peg point, which is located near the middle of the strip data (i.e., in the center of a pre-selected discrete latitude band).

We first consider an ascending orbit pass over the ocean to validate the use of ocean elevation data to correct for ripples (Figure 12). The data extends from the Bering Sea to the east of Alaska and near the coast of Bethel in the Kuskokwim Bay and covering some of the Pribilof Islands (Figure 12(e)). SRTM InSAR data over the ocean is ideal for visualizing height errors and HREC processing due to the regular and dense distribution of GCPs from ocean tide models from the original SRTM processing (Figure 12(a)). The ocean elevation over the 200,000 sq km area varies gradually between -1 and 17 meters. The noisier SRTM elevations generally follow the ocean topography but height ripples are also visible (Figure 12(c)).

The SRTM/GCP elevation difference image (Figure 12(b)) has a high-density distribution of accurate GCPs and allows us to observe several SRTM data characteristics:

- The four subswaths are visible (with borders at approximately -45, 10, and 65 km in range) and exhibit different levels of decorrelation and, therefore, different levels of random noise and height errors. The third beam is worse than the first and second beams (left), while the fourth beam (right) is the worst. The Beam 4 degradation is due to the larger incidence angle and the fact that it was acquired with the horizontal polarization. Beams 2 and 3 were acquired with vertical polarization.
- The antenna beam pattern effect is visible, as the noise level increases away from the antenna pattern centroid (e.g., in the areas between Beams 1 and 2, and between Beams 2 and 3). This and the previous effect are due to the changes in the SNR, which depends on incidence angle, polarization, and antenna beam pattern.

- A pronounced ripple is visible shortly below 0 km in the along-track distance. The typical ripple signature is observed in both the difference image (Figure 12(b)) and in the difference profile (Figure 12(d)). The ripple corresponds to the peak of the baseline roll angle (Figure 12(f)), at which the shuttle started attitude maneuvers to keep the baseline within the designated range. This type of height ripple motivates our use of an adaptive along-track window size that we reduce to at least 6 km to correct for the height ripple.
- Other systematic height errors are visible that may be related to attitude maneuvers of the shuttle but cannot be explained only by the inaccuracies of baseline roll angle estimation (as shown and discussed later in the section). Although the cause of the errors could come for errors in the GCP data, their magnitude is small. Most important is the fact that the observed errors are either random in nature (indicating random phase noise in SRTM data and in GCP data), and that all the systematic errors align with the radar range along-track dimensions. This, in fact, strengthens the argument that the observed systematic errors are only due to the SRTM height data and can be corrected given a dense enough coverage of GCPs.

As a second example, we consider an interior land area spanning a variety of terrain types, including mountains, hills, forests, and plains (Figure 13). The ~1,000 km ascending pass extends from the Rocky Mountains in Montana, USA, to the snow-covered plains of Saskatchewan in Canada (Figure 13(e)). The images demonstrate the spatial distribution of ICESat GCP points over interior land and the related errors (Figure 13(a)). Note that due to the orbit geometry, the density of ICESat GCPs increases away from the equator. In this example, the imaged area is in a relatively high northern latitude and exhibits a lidar shot density of 1.23 GCPs per sq km. Two large ripples are visible in the SRTM / GCP difference map (Figure 13(b)) and difference profile (Figure 13(d)) at along-track distances of approximately -280 km and +410 km. These locations correspond to shuttle thruster firings for attitude control maneuvers, as shown in the changes of the baseline roll angle (Figure 13(f)). One can also see the increased error variability in the southern part of the image over the mountains where both the SRTM and the ICESat GLAS data have larger errors.

The third example (Figure 14) shows height ripples over a coastal region in eastern Canada in a descending pass extending from Quebec to Newfoundland and covering the Anticosti Island in the Gulf of St. Lawrence (Figure 14(e)). This example exhibits height ripple effects caused by baseline estimation errors. The average error bias over this region is 41 cm with a standard deviation of 3.75 meters. Two ripples are visible in the SRTM / GCP difference map (Figure 14(b)) and difference profile (Figure 14(d)) at along-track distances of approximately -380 km and +300 km. These locations also correspond to shuttle thruster firings for attitude control maneuvers.

Finally, we show results of HREC processing for the three ripple examples: ocean (Figure 15), interior land (Figure 16), and coastal region (Figure 17). Three error correction models are applied and presented from left to right in the figures: the constant offset model (Equation 7), the slope model (Equation 5), and the linear model (Equation 9). The previously identified height ripples are significantly diminished using the slope model with the more general linear model also reducing systematic errors.

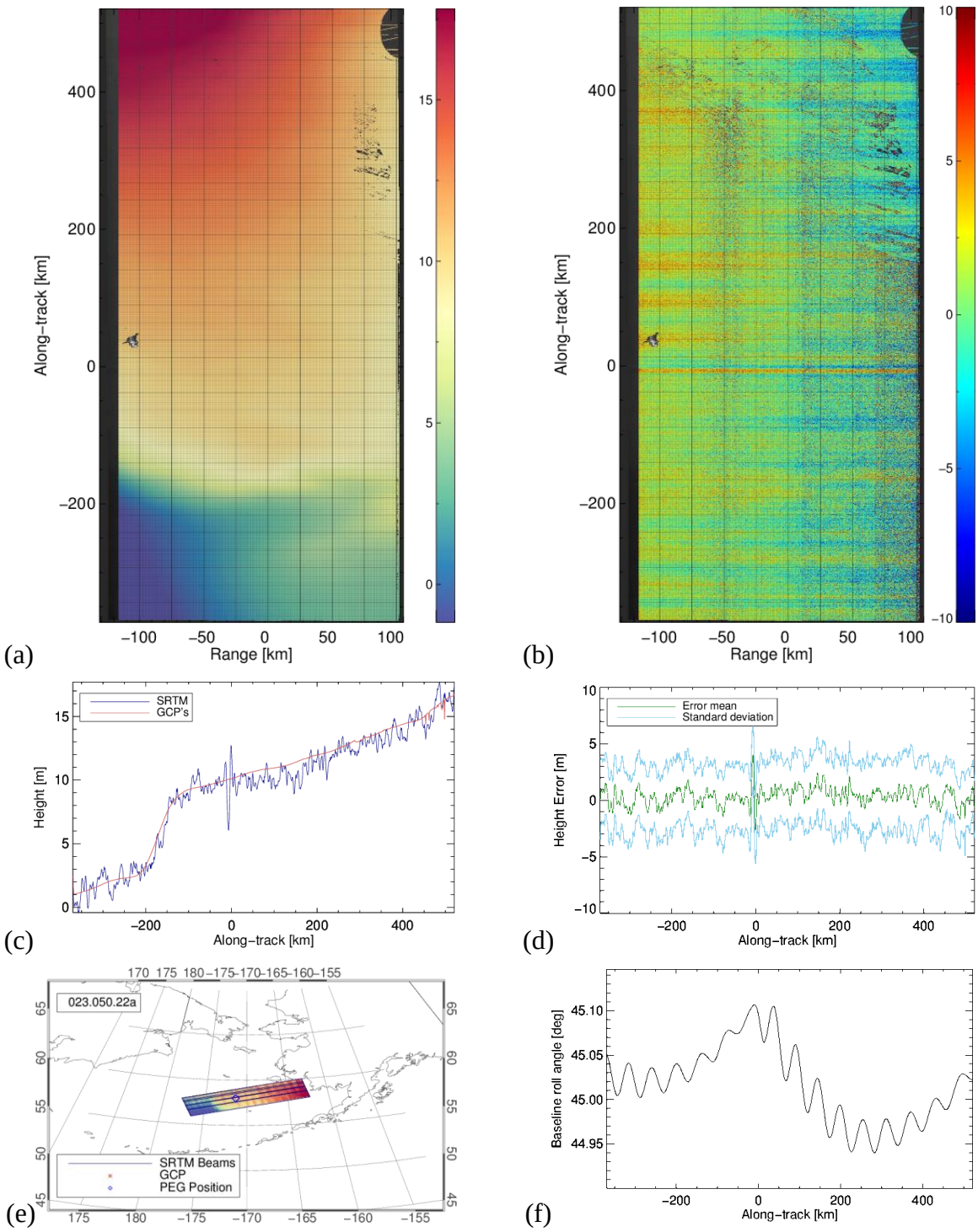

Figure 12. Example height ripples over ocean

(a) GCP elevations (color point cloud) displayed over SRTM elevations (gray raster). (b) SRTM / GCP elevation difference. (c) SRTM / GCP along-track elevation profiles averaged in range direction. (d) SRTM / GCP along-track elevation difference mean and standard deviation profiles for one-km along-track bins. (e) SRTM / GCP map coverage. (f) Baseline roll angle variations along-track.

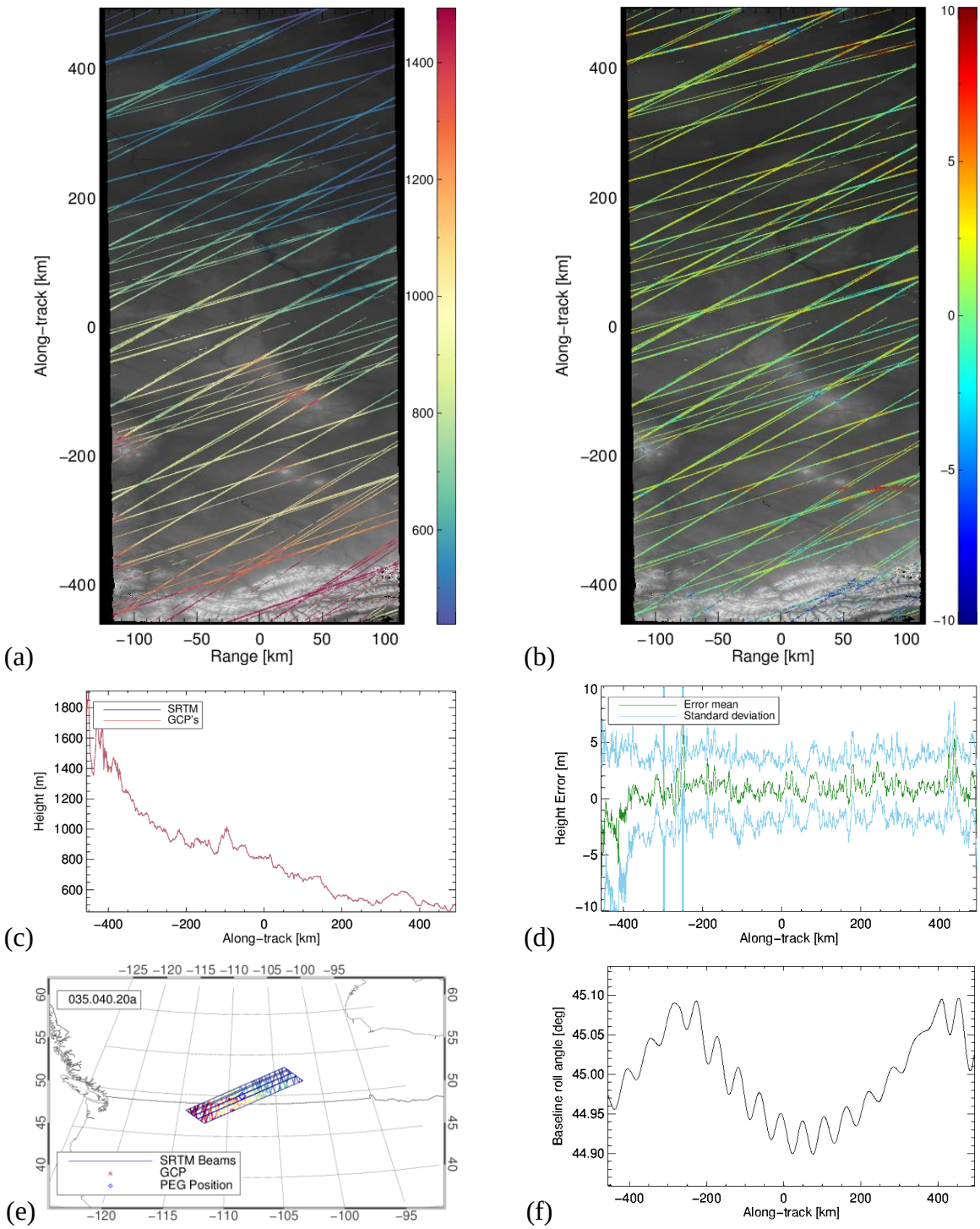

Figure 13. Example height ripples over interior land
(a) GCP elevations (color point cloud) displayed over SRTM elevations (gray raster). (b) SRTM / GCP elevation difference. (c) SRTM / GCP along-track elevation profiles averaged in range direction. (d) SRTM / GCP along-track elevation difference mean and standard deviation profiles for one-km along-track bins. (e) SRTM / GCP map coverage. (f) Baseline roll angle variations along-track.

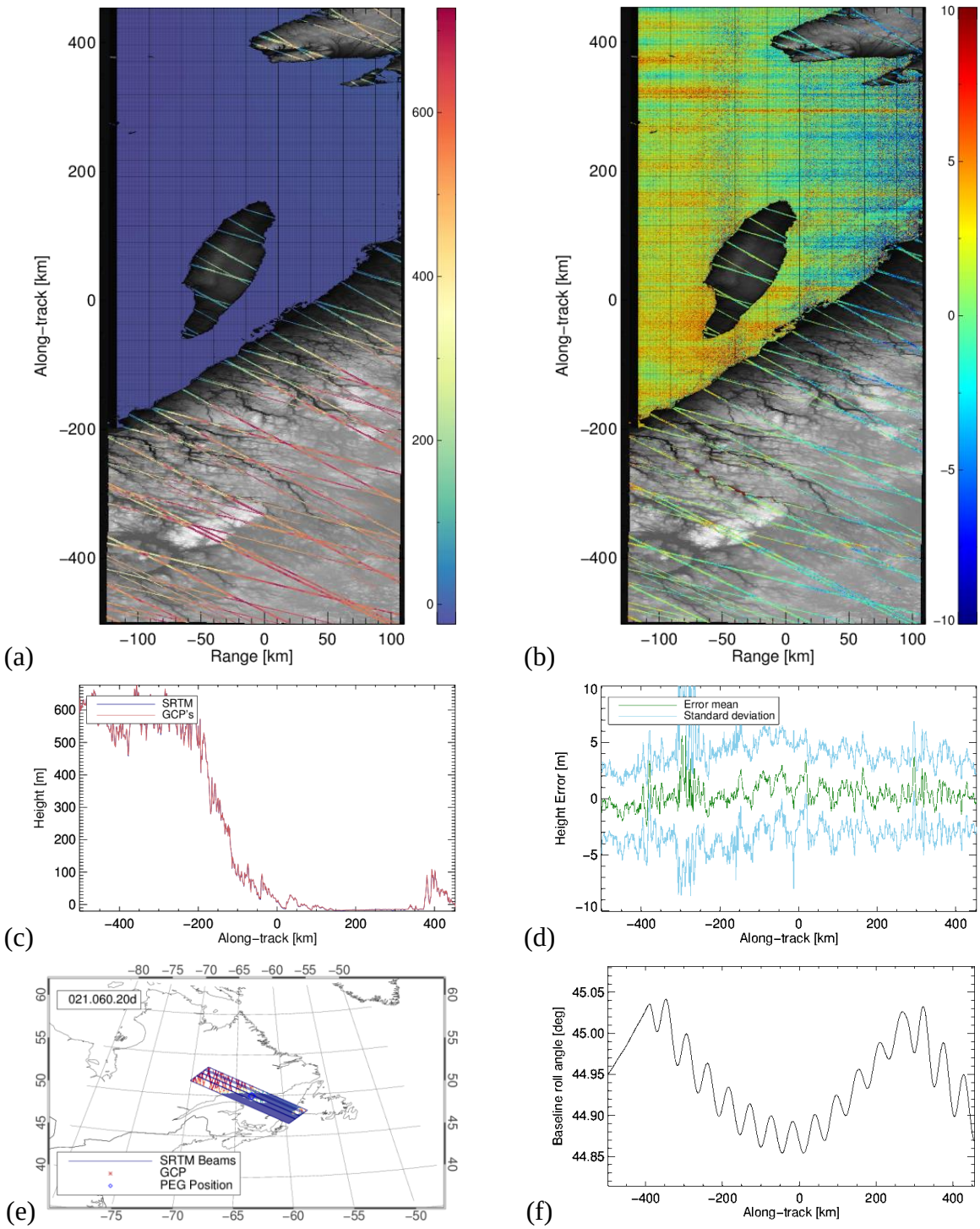

Figure 14. Example height ripples over a coastal region
(a) GCP elevations (color point cloud) displayed over SRTM elevations (gray raster). (b) SRTM / GCP elevation difference. (c) SRTM / GCP along-track elevation profiles averaged in range direction. (d) SRTM / GCP along-track elevation difference mean and standard deviation profiles for one-km along-track bins. (e) SRTM / GCP map coverage. (f) Baseline roll angle variations along-track.

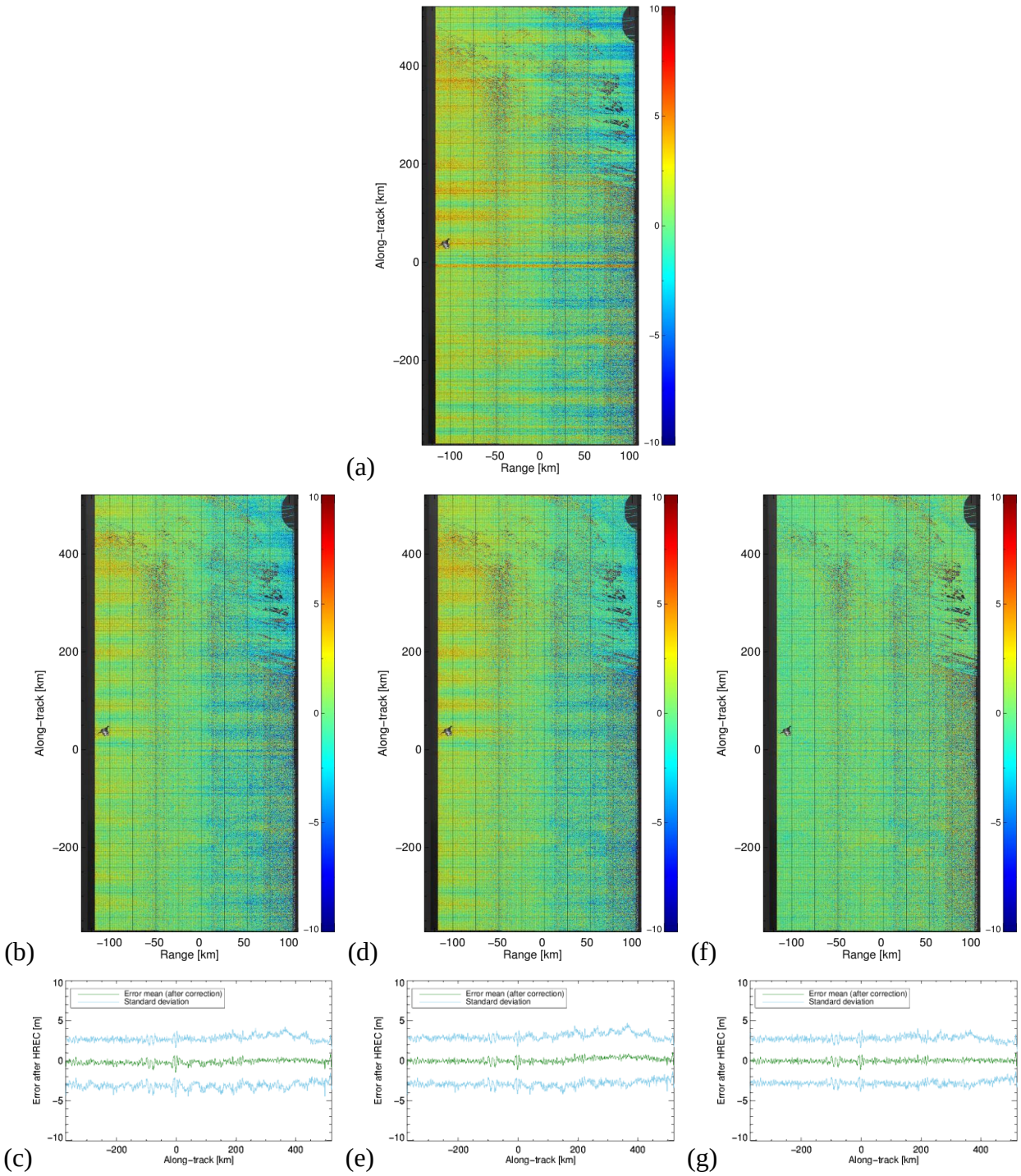

Figure 15. Correction results for ocean example
(a) SRTM / GCP elevation difference (Figure 12(b)). (b-c) Difference image and profiles after correcting with offset model (Equation 7). (d-e) Difference image and profiles after correcting with slope model (Equation 5). (f-g) Difference image and profiles after correcting with linear model (Equation 9).

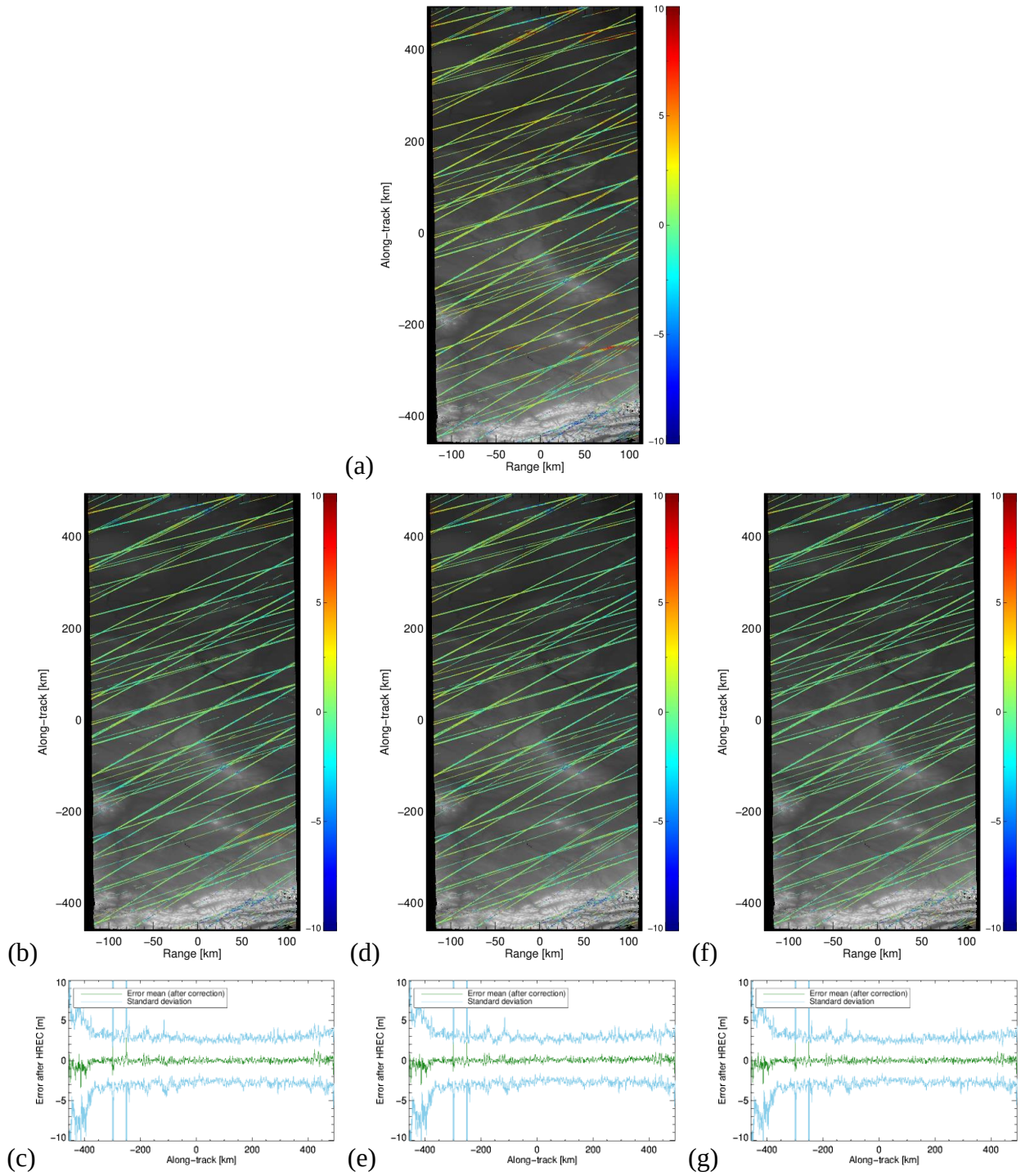

Figure 16. Correction results for interior land example
(a) SRTM / GCP elevation difference (Figure 13(b)). (b-c) Difference image and profiles after correcting with offset model (Equation 7). (d-e) Difference image and profiles after correcting with slope model (Equation 5). (f-g) Difference image and profiles after correcting with linear model (Equation 9).

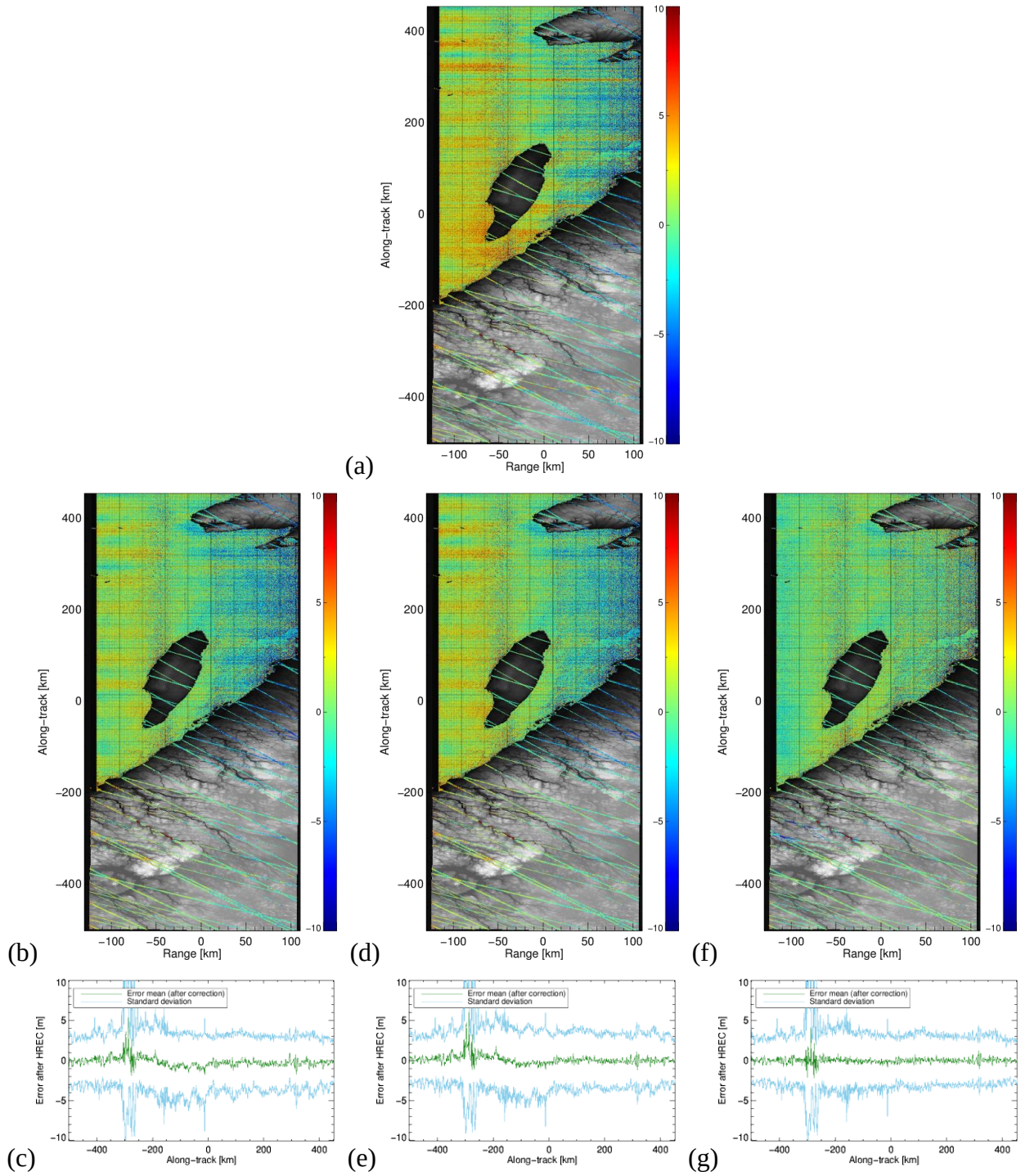

Figure 17. Correction results for coastal region example
(a) SRTM / GCP elevation difference (Figure 14(b)). (b-c) Difference image and profiles after correcting with offset model (Equation 7). (d-e) Difference image and profiles after correcting with slope model (Equation 5). (f-g) Difference image and profiles after correcting with linear model (Equation 9).

4.2.6 Continental Processing and Results

This section presents results of applying HREC to strip datasets over North America.

4.2.6.1 Data Coverage and Uncertainties

The NASADEM North America strip height data consists of 2,244 strip datasets of reprocessed SRTM data. The ICESat database for North America contains more than 10 million bare ground and 9 million vegetated lidar data points. The average ICESat data density is 1.4 lidar points per sq km. The ocean GCPs are provided on a 500-meter grid over large water bodies that are classified as ocean in the land-water mask, and cover all the coastal regions. Figure 18 shows the distribution of the number of GCPs per SRTM strip dataset as well as the distribution of strip area and the percentage of valid pixels inside the strips.

The distributions of uncertainties of ICESat bare ground and vegetated lidar elevation heights in North America are shown in the two left plots in Figure 19. As expected, the bare ground distribution is narrower with a lower mean uncertainty. The distribution of uncertainties of SRTM height estimates is shown in the right plot of Figure 19.

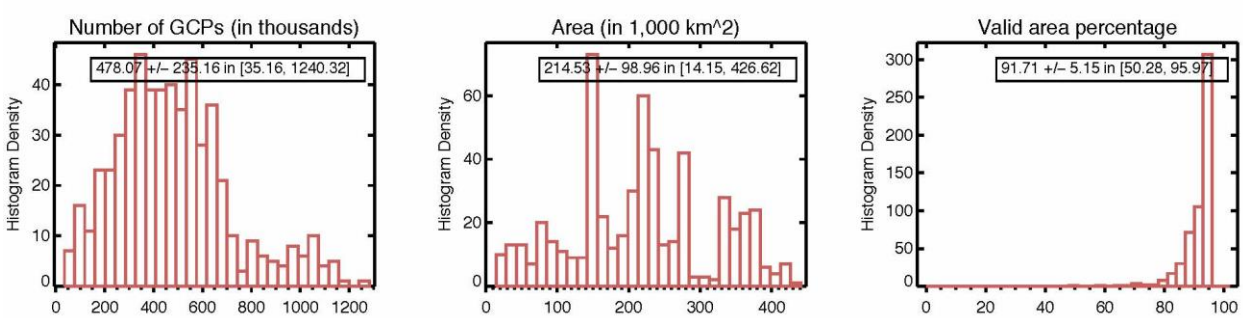

Figure 18. Coverage characteristic histograms for North America strip height datasets
(Left) Number of GCPs (in thousands) per SRTM strip height datasets. (Center) Strip image area (in thousands of square km). (Right) Valid pixels (in percent) in SRTM strip height datasets.

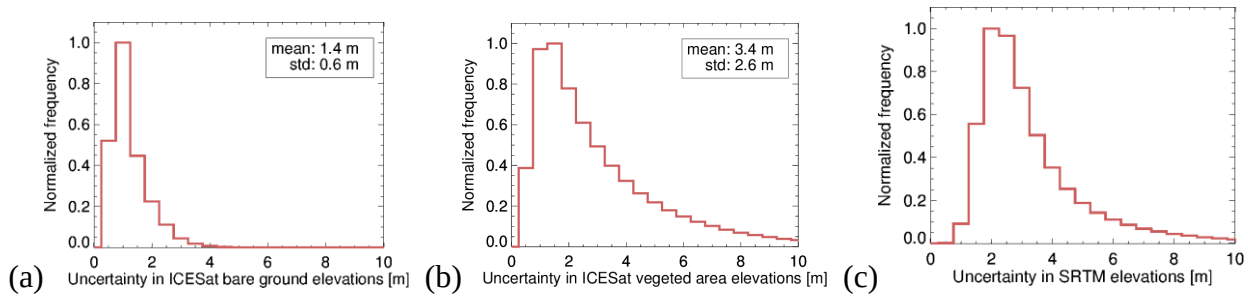

Figure 19. ICESat and SRTM elevation uncertainties for North America
(a) Error distribution for ICESat bare ground data (in meters). (b) Error distribution for ICESat vegetated area data (in meters). (c) Error distribution for SRTM data (in meters).

4.2.6.2 Continental Processing and Performance Evaluation

Applying HREC processing to the North America data allowed us to correct for the height ripples as well as to reduce other systematic height errors. For the linear correction function, the unweighted root mean square error (RMSE) was reduced from 6.1 m to 5.3 m. The weighted RMSE was reduced from 5.0 m to 4.0 m. The HREC linear model results are summarized in Table 5 and the distributions of the performance evaluation metrics are shown in Figure 20 (averaged per SRTM strip height dataset). Figure 21 shows the distribution of average estimated offset (in m) and slope (in cm per ground range km) per SRTM strip dataset. As is shown, the average height offset (b_0 in Equation 9) is 1.25 m with a standard deviation of 2.34 m. The average estimated slope (b_1 in Equation 9) is -0.7 cm per ground range km, with a standard deviation of 1 cm per km.

4.2.7 Conclusion

This section presented the approach for systematic height error correction of the global SRTM DEM as part of the NASADEM reprocessing based on control points from ICESat lidar shots and the modeled ocean topography. The approach nearly eliminates systematic errors caused by imprecise knowledge of the baseline attitude. It relies on a dense grid of accurate ground control points, which are weighted depending on their uncertainties. The challenges include certain terrain types with a lack of reliable ground control points, such as in mountainous regions with significant slopes where ICESat and SRTM elevation estimates are not as accurate, vegetation where ICESat and SRTM may have distinctive elevation measurements, and low backscatter areas. We mitigated potential error sources due to changes between acquisitions, such as vegetation growth, natural forest disturbances, ice and snow accumulation, or seasonal effects (e.g., glacier melt, snow cover, leaf on/off conditions) using auxiliary datasets. The ocean topography data proved accurate and reliable, enabling us to understand the error characteristics of SRTM data.

Table 5. North America HREC strip dataset performance using the linear model

	Mean	Std Dev	Min	Max
Number of GCPs per strip dataset	478,070	235,164	35,159	1,240,321
Mean absolute error before correction (m)	3.46	2.65	2.05	58.88
Mean absolute error after correction (m)	2.81	1.03	1.74	17.19
Root mean square error before correction (m)	6.08	7.18	2.73	84.98
Root mean square error after correction (m)	5.30	6.05	2.29	74.03

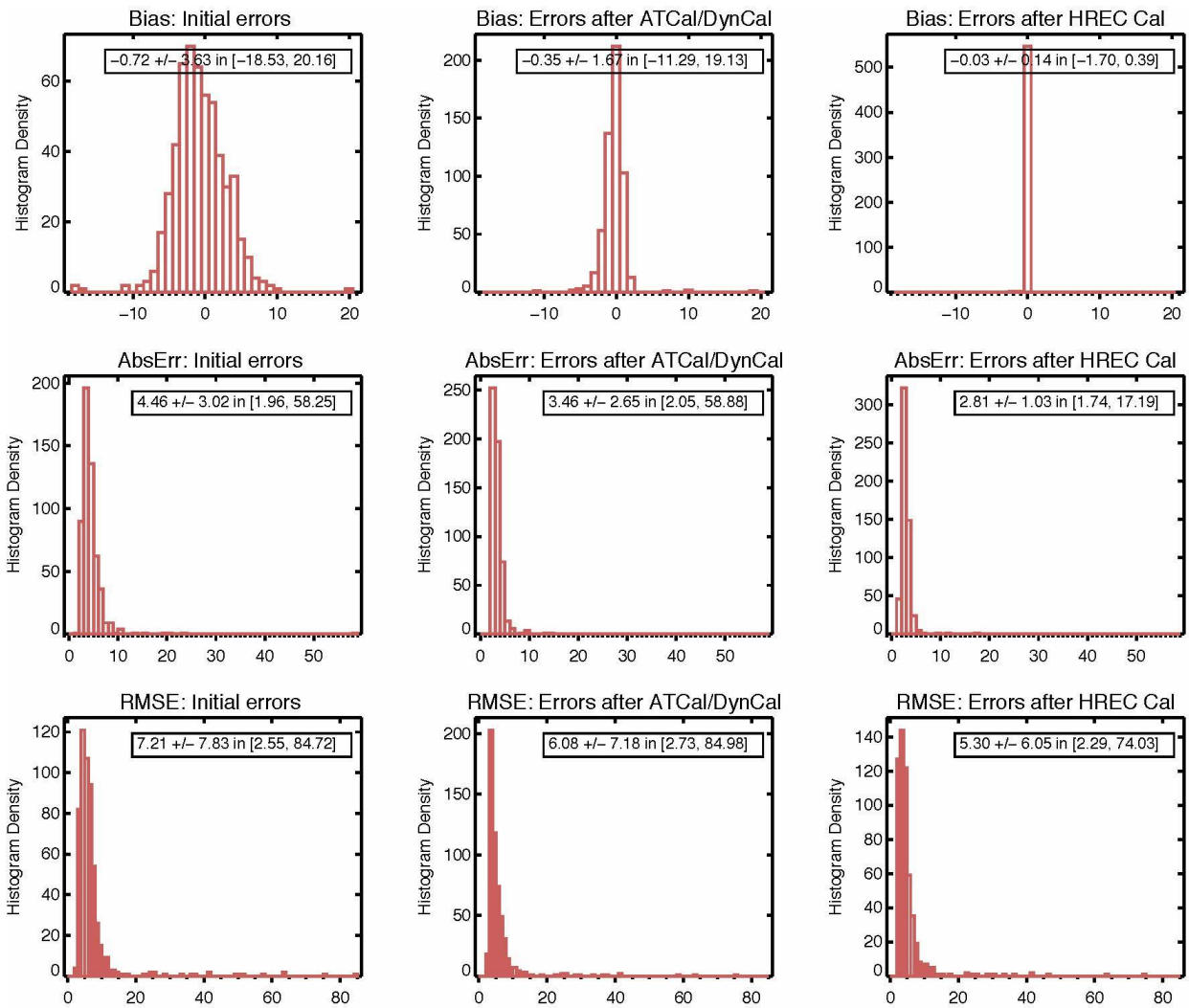

Figure 20. Histograms of average error characterisitics throughout North America processing
From top to bottom: Bias, absolute error, and RMSE evaluated after three processing steps: After initial SRTM height estimation (left), after SRTM along-track calibration (ATCal) and SRTM dynamic calibration (DynCal) processing steps (middle), and after NASADEM HREC processing step (right).

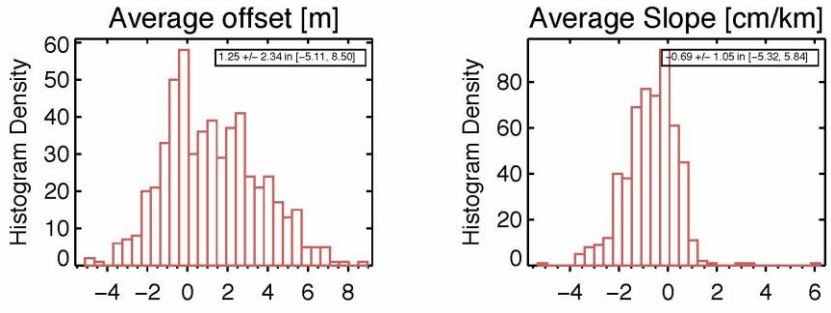

Figure 21. Histograms of HREC average offset and roll angle slope for North America
(Left) Offset (in m). (Right) Roll angle slope (in elevation height cm per ground range km).

4.3 Height Precision Estimation

We modified the SRTM processor to improve the error (i.e., height precision) estimation. The new implementation consists of a more accurate computation of the phase standard deviation than the Cramer-Rao lower bound used in the original processor and an improved estimate of the effective number of looks used in the processing filters and correlation estimator.

We improved on the Cramer-Rao lower bound formula by numerically evaluating the phase standard deviation from its known probability density function as a function of the interferometric correlation and the effective number of looks. This required a correlation correction to remove the known estimator bias. We pre-computed the correlation bias correction and phase standard deviation as a pair of two-dimensional tables on a uniformly spaced grid. The NASADEM processor used nearest-neighbor interpolation to obtain an unbiased correlation value at every pixel as a function of the biased correlation estimate and the effective number of looks of the estimator. Then we determined a phase standard deviation value at every pixel by look up as a function of the unbiased correlation and the effective number of looks.

5 NASADEM FINISHING

This section describes DEM merging and slope and curvature product generation.

5.1 DEM Merging

The creation of the final void-free NASADEM DEM required a number of DEM conditioning and merging steps described below.

5.1.1 Ellipsoid to Geoid Conversion

Most DEM users require elevations referenced to the geoid rather than referenced to the ellipsoid (i.e., with the oceans at zero elevation). Up to this point, the SRTM reprocessing was with reference to the WGS84 ellipsoid. The conversion to a geoid reference was done by first generating a floating-point conversion array at 15x15-arcsecond postings for latitude-longitude 50x50-degree tiles from a standard EGM96 database. These arrays were then resampled to 1x1-arcsecond postings by bilinear interpolation to produce an ellipsoid-to-geoid conversion array for each 1x1-degree SRTM quad. The conversion arrays were then differenced from each SRTM ellipsoid-referenced quad to produce each SRTM geoid-referenced quad.

5.1.2 Water Masking

Although SRTM could measure some water elevations, it had the usual side-looking radar problem of specular reflection, with little signal return from smooth water bodies. This was addressed in the original SRTM DEM by creating an ancillary water mask known as the SRTM Water Body Dataset (SWBD). The SWBD was produced by NIMA/NGA commercial using the SRTM DEM, SRTM radar imagery, and other sources of satellite imagery (e.g., Landsat) to

distinguish land from water (Slater et al., 2006). The SWBD was produced in a vector shoreline format. The SRTM Version 1 DEM contained SRTM water elevations and was not masked by SWBD. In the SRTM Version 2 DEM, oceans were set to zero elevation using the SWBD mask. Other standing water bodies (lakes) were flattened to a constant elevation estimated from the SRTM DEM, and rivers were flattened into monotonic integer steps intended to fit their shoreline terrain.

Inspection of the SRTM Version 2 DEM revealed that SWBD rivers did not always fit the surrounding terrain, particularly in rugged terrain. In some places, rivers cut through the terrain like a gorge (but where no gorge exists) or are above the terrain. The shoreline terrain can be significantly (several meters, often 10m) below the river, which is an unnatural situation in most terrains. The source of these problems was a major target of this NASADEM project, as described above. Each SRTM data swath was adjusted vertically to be more consistent with ICESat profiles. This reduced warps in the new SRTM DEM that were revealed in the original SRTM DEM by flat or monotonic water bodies.

With many of the original SRTM DEM warps removed or reduced, we adjusted the SWBD-masked water elevations of the SRTM Version 2 DEM to fit the new SRTM DEM. First, we rasterized SWBD and surveyed it for errors. Then we used it to adjust the new SRTM DEM water body elevations.

The SWBD was rasterized into a binary land-versus-water mask. We found the mask did not perfectly match the SWBD mask used for SRTM Version 2 but we could not determine the cause of the minor local differences. Significant errors in the SWBD, as evident in both the SRTM Version 2 DEM and in our rasterized SWBD, generally did match. These were often protrusions from islands having the appearance of “giant wharfs.” Some others were gaps in major rivers. We used the GDEM3 water mask (produced by Sensor Information Laboratory Corporation in Japan) as a guide to repair many of these SWBD errors in approximately 140 quads.

Next, a best-fit procedure was used to match each lake and river segment to its surrounding shores. The original SWBD creation and application cost several million dollars and involved labor and cost-intensive procedures that could not be replicated within the NASADEM budget. Consequently, the NASADEM procedure was designed to adjust the water level to be consistent with the adjustments of the surrounding terrain. In some locations, this lost the river monotonicity that had been enforced with SRTM Version 2. We adjusted each lake and river segment vertically by comparing the average elevation of its shore in the new SRTM DEM to that in SRTM Version 2. Pixels immediately adjacent to the SWBD were avoided due to the imperfect match of the original SWBD and the new NASADEM SWBD. Instead, pixels approximately three pixels landward from the SWBD were used for comparison.

Multi-quad water bodies required special handling. For the Great Lakes of North America, the Caspian Sea, and other such large water bodies, a best-fit elevation was selected and applied manually. As with the SRTM Version 2 DEM, shoreline pixels and any land pixels touching the side or corner of any water pixel were set to the water elevation plus one meter if not already higher than the water.

Although not related to water masking, another error reduction applied at this stage of processing was to replace any SRTM pixel with the average of its eight neighboring pixels if it differed from that average by more than 100 meters. Along with water masking, this was another DEM “finishing” step originally applied in the generation of SRTM Version 2 (Slater et al., 2006). We did not extensively evaluate the need for this step but found it to be significant in a few quads.

5.1.3 Unwrapping Error Detection and Removal

Radar interferometry DEM generation is subject to phase unwrapping errors in which some areas of the DEM are too high or too low in elevation. As is evident in the SRTM DEM, this occurs near voids (i.e., near areas where the attempted unwrapping failed to produce a reliable elevation result). More specifically, an unwrapping error is typically an area nearly surrounded by a void, having only a few pixels connecting it to an area of correct elevations.

Except in regions with mesas (flat-topped, steep-sided hills), most unwrapping errors are areas of elevations that are too high. These typically occur in step-sided canyons. In order to detect these errors in the new SRTM DEM, we mapped areas in which SRTM elevations were more than 120 meters higher than corresponding pixels in GDEM2. Each quad with numerous such pixels was displayed for inspection in order to confirm the presence of an unwrapping error. Confirmation consisted of the typical void and limited pixel connection pattern and an unnatural geomorphology. Unwrapping errors were found in 158 quads and were voided manually by creating a mask with an onscreen graphics tool. The mask was then used to void the new SRTM DEM data.

Note that most errors in GDEM2 are related to clouds. Therefore, SRTM unwrapping errors could not be detected by mapping areas where the SRTM DEM is significantly lower than GDEM2. However, those areas are believed to be relatively rare.

5.1.4 ASTER GDEM, ALOS PRISM AW3D30 DEM, and Void Filling

The original plan for NASADEM was to fill voids of the reprocessed SRTM DEM with ASTER Global DEM 2 (GDEM2), any forthcoming ASTER GDEM, and possibly other publicly available DEMs. We previously used GDEM2 and GMTED2010 (Danielson and Gesch, 2011) to create NASA SRTM Version 3, also known as SRTM Plus. Some errors in GDEM2 were suppressed in SRTM Plus, but our plan was to improve the suppression of errors in GDEM, if possible. (Note: NASA SRTM Version 3 is not to be confused with “SRTM Versions 3 and 4” produced by CGIAR as their own follow-on DEMs to the NASA JPL and NIMA/NGA produced SRTM Versions 1 and 2.)

Well into the NASADEM project, the ALOS World 3D 30-meter (AW3D30) DEM (Tadono et al., 2016) was released, and we judged it to be of value for SRTM DEM void filling and GDEM error detection. Ultimately, we used only the GDEMs, the PRISM AW3D30 DEM, and interpolation for void filling. We did not use GMTED2010 or any other DEMs.

It is worth noting that our reprocessed SRTM DEM, the GDEMs, and the PRISM AW3D30 DEM all have some mutual dependency. The SRTM DEM reprocessing referenced an updated low-resolution database that included much GDEM2. The GDEMs used SRTM DEMs for error checking and void filling (especially in cloud-prone areas). The PRISM AW3D30 DEM used the SRTM DEM for error checking and vertical adjustments. Not surprisingly, part of creating each improved global DEM involves referencing and utilizing the strengths of each previous global DEM.

The ASTER GDEMs are derived from the ASTER sensor on the NASA Terra satellite, using its stereoscopic bands 3N (nadir) and 3B (back-looking) at 0.76 to 0.86 micrometer near-infrared wavelengths. ASTER is a cooperative effort between NASA, the Japan Ministry of

Economy, Trade and Industry (METI), and Japan Space Systems. GDEMs are a production of Sensor Information Laboratory Corporation (SILC, Japan). GDEM was first released in 2009, but was superseded in 2011 by GDEM Version 2 (GDEM2) (Fujisada et al., 2011, 2012), which had finer resolution and fewer errors. A variety of further improvements are leading to GDEMv3. These were implemented by SILC during 2015-2017 and included suggestions from our NASADEM assessments. Additional improvements implemented by us, as described below and used here, are part of the pending public release of GDEMv3.

The AW3D DEM with a 0.15-arcsecond (~5m) pixel spacing was produced by the Japan Aerospace Exploration Agency (JAXA) and its collaborators using imagery from the Panchromatic Remote-sensing Instrument for Stereo Mapping (PRISM) onboard the Advanced Land Observation Satellite (ALOS). The panchromatic wavelength is 0.52-0.77 micrometers (visible green and red, and near-infrared). JAXA also resampled much of the AW3D to one-arcsecond pixel spacing (~30m), like the SRTM DEM and the GDEMs, and called it AW3D30. Here, for clarity, we refer to it as PRISM AW3D30. While the SRTM DEM and the GDEMs have 3601x3601 pixels per 1x1-degree quad with overlap at quad edges, the PRISM AW3D30 DEM has 3600x3600 pixels per 1x1-degree quad with no overlap at quad edges. In other words, the pixel centers are offset half a pixel in latitude and longitude in the PRISM AW3D30 DEM versus the other DEMs. In order to bring the PRISM AW3D30 DEM into registration with the other DEMs we resampled most of it by cubic convolution. We also used bilinear interpolation at void edges to retain additional PRISM AW3D30 DEM coverage.

After some experimentation and evolution of methods, it was decided that our best approach to filling the voids of the reprocessed SRTM DEM was to create a void-free and error-suppressed new GDEM. Three unreleased drafts of GDEM3 from SILC were available to us via the ASTER Science Team. We produced a new error-suppressed void-free GDEM3 by (1) locating and masking errors in a draft GDEM3, (2) locating and masking errors in GDEM2, (3) similarly refining the PRISM AW3D30 DEM, and (4) merging these three DEMs and some of the reprocessed SRTM into a refined draft GDEM3. The final error-suppressed void-free GDEM3 then became the void-fill DEM for the reprocessed SRTM DEM of NASADEM. We will now discuss the processing in more detail.

5.1.5 GDEM Error Mask Generation

The GDEM error mask was created in three major steps. First, the input GDEM was compared to SRTM and PRISM AW3D30 for reasonable consistency. Second, the input GDEM was evaluated for the likelihood of errors (such as clouds) based upon its own morphology. Third, the composite mask generated from the first and second steps was expanded by filtering to include all input GDEM error pixels.

The first step followed qualitative logical probabilities. SRTM has no cloud errors, and the cloud avoidance for PRISM AW3D30 appears to be more consistently effective than the cloud avoidance of the input GDEM. However, both SRTM and PRISM AW3D30 have data voids, so are not always available for comparison with the input GDEM. Also, SRTM can have interferometric unwrapping errors, although the most significant of those were likely detected and were voided prior to comparison to the input GDEM. In short, SRTM is generally considered reliable and PRISM AW3D30 is considered less error-prone than the input GDEM especially

where two or fewer ASTER scenes (the "NUM" count) were used to create GDEM. With that in mind, this first step in creating the GDEM error mask utilized the following logic:

- If SRTM and PRISM AW3D30 not void, then the input GDEM pixel was rejected if it differed from both SRTM and PRISM AW3D30 by more than 80m.
- If SRTM and PRISM AW3D30 both void, then the input GDEM was not rejected.
- If SRTM void but PRISM AW3D30 not void, then the input GDEM was rejected if more than 80m different from PRISM AW3D30, unless the input GDEM NUM was 3 or more.
- If PRISM AW3D30 void but SRTM not void, then the input GDEM was rejected if more than 80 meters different from SRTM.

An initial rejection mask was thus created. The 80-meter threshold was determined empirically from extensive observational experience worldwide, maximizing cloud masking while minimizing the loss of obviously real topography such as dendritic erosion patterns. Subsequently, the mask was expanded to the eight neighboring pixels of any masked pixel in order to cover problem areas with the mask.

In the second major step, the mask was expanded to any pixel that differed "too much" from any neighboring pixel (thus having a slope so high as to be more likely an error, such as a cloud edge, than to be natural topography). The threshold for "too much" was defined as greater than 100 meters in the north-south or east-west direction at the equator, and it was defined as 141 (about the square root of 2 times 100) meters in the northwest-southeast and northeast-southwest directions at the equator. Exceeding the threshold in any one direction resulted in GDEM pixel masking. The thresholds were decreased appropriately as a cosine function of latitude for all orientations (except north-south) because longitude one-arcsecond pixel spacings decrease with latitude. As with the first step, the 100-meter threshold for the second step was determined empirically from extensive observational experience. Lower thresholds lost too much good topography and higher thresholds accepted too many cloud errors.

At this point, we had created a mask based upon the first two major steps: (1) comparisons of individual pixels to themselves in other datasets, and (2) comparisons of individual GDEM pixels to their immediate GDEM neighbors. However, neither of these steps extended across significant geography. That was found to be a problem. Often edges of clouds were masked but not the cloud interiors, which could be much less steep. Thus, a third major step, spatial filtering, was needed to fill in the mask.

Extensive testing resulted in the following effective filtering method. Any non-masked pixel was added to the mask if masked pixels were found within a 50-pixel radius in at least 12 of 16 "spoke" directions (north, south, east, and west, and approximately north-northwest, northwest, west-northwest, etc.). The concept here is that small areas need to be additionally masked if they are enclosed by masked pixels or if they are almost (at least 12/16) enclosed by masked pixels. Note that this method does not expand the exterior edges of masked regions (i.e., areas clearly exterior to clouds are preserved as unmasked).

A 5x5 median filter of the binary masked/not masked pixels was needed to avoid some noise from the 16 "spokes" of the detector. Pixels previously identified as too steep were then

restored to the mask where eliminated by the 5x5 median filter. The mask was then complete and found to be highly effective.

The masking of errors in GDEM creates voids that need to be filled. Preferably, these voids are filled with an alternative DEM rather than via interpolation. For consistency, the best DEM to fill the latest GDEM is an earlier GDEM. That results in a final GDEM that is maximally from ASTER and thus most inherently an ASTER product (i.e., without too much elevation that is already available to users from other sources). Using GDEM2 (the older GDEM) to fill the newer GDEM is possible because errors in the newer GDEM (the draft GDEM3) were not always spatially coincident with errors in GDEM2. The newer GDEM uses all ASTER scenes used in GDEM2 plus additional, more recent scenes. In general, having more scenes results in fewer errors. However, this is not always the case. Adding more cloudy scenes sometimes created errors in the newer GDEM that did not occur in the older GDEM.

Thus, we used GDEM2 as the elevation model of first choice for filling the newer GDEM. However, since GDEM2 has errors too, we first used the same error masking procedure on GDEM2 that we applied to the newer GDEM. SRTM, where available, was then the elevation model of second choice to be used as fill GDEM, noting that it has been the primary fill for all prior versions of GDEM. As described above, some interferometric unwrapping errors were removed from SRTM but no further masking was applied. PRISM AW3D30, where available, was then used as third choice, after it was subjected to a masking routine similar to that applied to the GDEM elevation models. Masking PRISM AW3D30 was a precautionary step. The need for such masking was not fully evaluated but was noted as beneficial in some locations. In particular, PRISM AW3D30 was additionally masked where its “stack” (scene count) number was zero, meaning the PRISM AW3D30 DEM was filled by interpolation. Oceans were also “installed” in PRISM AW3D30 (elevation set to zero) where SRTM, GDEM2, and the new GDEM (where any were available) were all ocean. Note that after masking GDEM2, all of the filler elevation models had voids (GDEM2, SRTM, and PRISM AW3D30), either inherently or from masking, or both.

Our void fill routine is a modified version of the Delta Surface Fill method of Grohmann et al. (2006). We modified the published method in order to (1) use filler DEMs with voids, (2) reduce the spread of errors from void edges into the void fill, and (3) improve processing speed.

In simple terms, the original Delta Surface Fill method was intended to create a void-free DEM from (1) a primary DEM that has voids and (2) a secondary DEM that does not have voids. The secondary DEM fills the voids seamlessly by being adjusted vertically to compensate for height differences (the delta) between the DEMs, with particular focus on the void edges in the primary DEM. Elevations of the secondary DEM within the voids of the primary DEM (where deltas can only be estimated) are adjusted vertically by deltas interpolated from those void edges. Thus, a full delta surface (the DEM difference) is calculated as a simple subtraction where outside the voids, and it is filled by interpolation within the voids. That void-free delta surface is the spatially variable vertical shift that is applied to the filler DEM as it fills the voids of the primary DEM.

As implemented for some steps (not the final step) for NASADEM, the delta surface has voids not only from the primary DEM but also from the secondary (filler) DEMs. This often means that some elevations (including void edges) in the primary DEM correspond to voids in the secondary DEM. This is not a severe problem because all of the delta surface values across a region should be nearly a constant, unless the DEMs are badly corrupted. The delta surface measures general vertical differences between the DEMs (such as reference datum errors, which are spatially

constant), various possible warps, and local vertical differences between the DEMs (associated with measurement errors of individual or neighboring pixels, thus having high spatial frequencies and no widespread trends). In short, estimating delta surfaces for voids in the primary DEM is usually performed by interpolation of the delta surface from the edges of those voids. However, if it is performed by interpolation from further away, namely at the edge of the void of the filler DEM, there is usually no large adverse impact. The fill may be somewhat less seamless at the edge of the void in the primary DEM, but that seamlessness may just have been corruption of the fill to better match errors at the void edge. It may look smoother but be less correct in terms of actual elevations. Thus, applying the Delta Surface Fill method with a filler-DEM that has voids does work, but it will leave remnant voids where both DEMs are void.

The delta surface is typically quite noisy. The vast majority of the elevation signal is cancelled and only differences (e.g., errors and possibly temporal differences) in the elevation measurements remain. Systematic errors (i.e., reference datums and warps) will remain, and these are what the delta surface is intended to extract and then suppress in the DEM merger. However, random errors also exist pixel-by-pixel or over small areas. This may be especially true at void edges next to pixels that were voided because they were clearly erroneous or at least unreliable. Interpolation from void edge pixels can therefore result in a delta surface fill that is particularly noisy. To suppress this, we applied a 5x5 median filter to the non-void pixels (only near voids, for speed). Interpolation across the delta surface voids then proceeded using these filtered void-edge pixels.

However, the delta elevations are typically still quite noisy, so an interpolation method is needed that suppresses local noise and keeps it local. Consequently, we used a repetitive edge growing interpolator. Pixels in the void directly adjacent to the void edge were interpolated, and then the void pixels next to those were interpolated from the first interpolated pixels. The edge growing interpolator was run for five iterations. This greatly smoothed the void fill. For speed in global processing, remaining void pixels used direct interpolation and skipped edge growing.

In both the edge growing interpolator and the interpolator without edge growing, we used an inverse square root of distance interpolator that looked in 16 directions (north, south, east, west, and approximately west-northwest, northwest, north-northwest, etc.). Using the inverse square root of distance may be unique. Interpolators often use the inverse square (not square root) of distance to more heavily weight nearby reference points, especially the single nearest reference point. However, we wanted, to some degree, the opposite. We wanted to de-emphasize noise in the very nearest reference points. Distant pixels are generally less relevant in most interpolations. However, recall that the delta surface generally measures a fairly uniform value (i.e., the elevation signal cancels out). Distant reference pixels are more scattered and therefore less redundantly subject to a single noise source. Giving distant pixels extra weighting helps to reduce noise. This is particularly true in the edge-growing interpolator because typically half of the 16 look directions find pixels that are only a very few pixels away, and close pixels (due to their quantity) already are heavily weighted because of that. The inverse square root of distance formula helps balance the weighting of reference points around the void.

With the delta surface calculated and filled, the combined DEM is generated via these logical steps:

1. The output is the primary DEM where it exists.

2. The output is void where both DEMs are void.
3. The output is the secondary DEM shifted by the filled delta surface where the primary DEM is void and the secondary DEM is not void.

5.1.6 Remaining DEM Merging Steps

The remaining processing steps included despiking GDEM2 and GDEM3, merging the secondary DEMs into the new SRTM, and edge matching the final NASADEM DEM.

5.2 Slope and Curvature

We created a slope and curvature module (SCM) to generate the NASADEM slope, aspect angle, profile curvature and plan curvature products. This section describes the input data, surface fitting process, and output product calculations.

5.2.1 Input Data

SCM takes as input a final void-free terrain height data file and the corresponding NUM and height precision error files. The NUM file is used to identify the source of the DEM posting as part of assigning weights in the surface fitting process. The eight neighboring cells are also used to pull in data for edge pixel calculations.

For each output posting, the input latitude/longitude height DEM data expressed in the WGS84 datum are converted to an East-North-Up (ENU) Cartesian coordinate system centered on the output posting. The conversion is done to leading order:

$$E = R_N \Delta\lambda \cos\phi \tag{11}$$

$$N = R_M \Delta\phi \tag{12}$$

$$U = z - \frac{z}{2}\left(\frac{\Delta\lambda^2}{R_N} + \frac{\Delta\phi^2}{R_M}\right) \tag{13}$$

where R_M and R_N are the meridional and normal radii of curvature at the origin and the input data coordinates are expressed as differences $\Delta\phi$ and $\Delta\lambda$ with respect to the output posting latitude ϕ and longitude λ .

5.2.2 Surface Fitting

The local surface is fit with a weighted paraboloid (quadric):

$$z = f(x, y) = p_0 x^2 + p_1 xy + p_2 y^2 + p_3 x + p_4 y + p_5 \tag{14}$$

Weighted best-fit surfaces are computed by inverting the matrix equation:

$$\left(\sum_{i=1}^{N} \mathbf{Q_i} \mathbf{Q_i^T} \right) \mathbf{P} = \left(\sum_{i=1}^{N} z_i \mathbf{Q_i} \right) \tag{15}$$

for the fit coefficients

$$\mathbf{P} = \begin{bmatrix} p_0 & p_1 & p_2 & p_3 & p_4 & p_5 \end{bmatrix} \tag{16}$$

where the accumulation matrices are

$$\left(\sum_{i=1}^{N} \mathbf{Q_i} \mathbf{Q_i^T} \right) = \begin{bmatrix} s(x^4) & s(x^3 y) & s(x^2 y^2) & s(x^3) & s(x^2 y) & s(x^2) \\ s(x^3 y) & s(x^2 y^2) & s(xy^3) & s(x^2 y) & s(xy^2) & s(xy) \\ s(x^2 y^2) & s(xy^3) & s(y^4) & s(xy^2) & s(y^3) & s(y^2) \\ s(x^3) & s(x^2 y) & s(xy^2) & s(x^2) & s(xy) & s(x) \\ s(x^2 y) & s(xy^2) & s(y^3) & s(xy) & s(y^2) & s(y) \\ s(x^2) & s(xy) & s(y^2) & s(x) & s(y) & s(1) \end{bmatrix} \tag{17}$$

$$\left(\sum_{i=1}^{N} z_i \mathbf{Q_i} \right) = \begin{bmatrix} s(zx^2) \\ s(zxy) \\ s(zy^2) \\ s(zx) \\ s(zy) \\ s(z) \end{bmatrix} \tag{18}$$

and the notation

$$s\left(z^p x^n y^m\right) = \sum_{i=1}^{N} z_i^p x_i^n y_i^m w_i \tag{19}$$

represents the weighted moment computed from the N (x, y, z) postings.

5.2.3 Slope and Curvatures

The NASADEM slope S and aspect angle ϕ are determined from the fitted surface function $f(x, y)$ from Equation 14:

$$S = \sqrt{f_x^2 + f_y^2} \tag{20}$$

$$\phi = \arctan\left(\frac{f_y}{f_x}\right) \tag{21}$$

where f_x and f_y are the partial derivatives with respect to x and y, respectively, and are computed from the quadric fit coefficients. The aspect angle is measured clockwise from north.

The NASADEM profile & plan curvature definitions follow the conventions established in Peckham (2011). The profile curvature $c_{profile}$, also called the vertical curvature, is computed as:

$$c_{profile} = \frac{-\left(f_x^2 f_{xx} + 2 f_x f_y f_{xy} + f_y^2 f_{yy}\right)}{S^2\left(1 + S^2\right)^{3/2}} \tag{22}$$

and is defined by differential movements along the streamline curve on the three-dimensional surface. The plan curvature c_{plan}, also called the contour curvature or the horizontal curvature, is:

$$c_{plan} = \frac{-\left(f_y^2 f_{xx} - 2 f_x f_y f_{xy} + f_x^2 f_{yy}\right)}{S^3} \tag{23}$$

The software has modules for verifying that the entire process works. These are non-production modules and are independently coded. For example, we created an analytics module that makes DEMs from analytic functions and independently computes the slope, aspect angle,

plan curvature, and profile curvature. Then it runs the production code on the analytic DEM so that production data products can be compared with their analytically computed counterparts.

6 ACKNOWLEDGMENTS

Copyright 2020 California Institute of Technology. The research was carried out at the Jet Propulsion Laboratory, California Institute of Technology, under a contract with the National Aeronautics and Space Administration. Funding provided by the NASA Making Earth System Data Records for Use in Research Environments (MEaSUREs) program. Resources supporting this work provided by the NASA High-End Computing (HEC) Program through the NASA Advanced Supercomputing (NAS) Division at Ames Research Center.

7 DATA ACCESS

NASADEM products are available through the Land Processes Distributed Active Archive Center (LP DAAC) through NASA Earthdata Search & the Data Pool. Many of the GIS software packages used to ingest previous SRTM products can be used to work with NASADEM data.

8 CONTACT INFORMATION

Contact information for LP DAAC User Services: lpdaac@usgs.gov

9 ACRONYMS

ALOS	Advanced Land Observation Satellite
ASTER	Advanced Spaceborne Thermal Emission and Reflection Radiometer
AW3D30	ALOS World 3D 30-meter DEM
DAAC	Distributed Active Archive Center
DEM	Digital Elevation Model
DN	Digital Number
GCP	Ground Control Point
GDEM	Global Digital Elevation Model products derived from ASTER data
GIS	Geographic Information System
GLAS	Geoscience Laser Altimeter System
ICESat	Ice, Cloud, and Land Elevation Satellite
InSAR	Interferometric Synthetic Aperture Radar
LP	Land Processes
PRISM	Portable Remote Imaging Spectrometer
SAR	Synthetic Aperture Radar
SNR	Signal-to-Noise Ratio

10 REFERENCES

Arendt, A., Bliss, A., Bolch, T., Cogley, J., Gardner, A. S., Hagen, J.-O., Hock, R., Huss, M., Kaser, G., Kienholz, C., Pfeffer, W., Moholdt, G., Paul, F., Radic, V., Andreassen, L., Bajracharya, S., Barrand, N., Beedle, M., Berthier, E., Bhambri, R., Brown, I., Burgess, E., Burgess, D., Cawkwell, F., Chinn, T., Copland, L., Davies, B., Angelis, H. D., Dolgova, E., Earl, L., Filbert, K., Forester, R., Fountain, A. G., Frey, H., Giffen, B., Glasser, N., Guo, W., Gurney, S., Hagg, W., Hall, D., Haritashya, U., Hartmann, G., Helm, C., Herreid, S., Howat, I., Kapustin, G., Khromova, T., Koenig, M., Kohler, J., Kriegel, D., Kutuzov, S., Lavrentiev, I., LeBris, R., Liu, S., Lund, J., Manley, W., Marti, R., Mayer, C., Miles, E., Li, X., Menounos, B., Mercer, A., N. Moelg, P. M., Nosenko, G., Negrete, A., Nuimura, T., Nuth, C., Pettersson, R., Racoviteanu, A., Ranzi, R., Rastner, P., Rau, F., Raup, B., Rich, J., Rott, H., Sakai, A., Schneider, C., Seliverstov, Y., Sharp, M., Sigurosson, O., Stokes, C., R.G.Way, R.W., Winsvold, S., Wolken, G., Wyatt, F., & Zheltyhina, N. (2015). Randolph Glacier Inventory: A Dataset of Global Glacier Outlines: Version 5.0. Global Land Ice Measurements from Space. Boulder Colorado, USA.

Bamler, R., & Hartl, P. (1998). Synthetic aperture radar interferometry. Inverse Problems, 14 , R1-R54.

Bhang, K. J., Schwartz, F. W., & Braun, A. (2007). Verification of the vertical error in C-band SRTM DEM using ICESat and Landsat-7, Otter Tail County, MN. Geoscience and Remote Sensing, IEEE Transactions on, 45, 36-44.

Carabajal, C. C., & Harding, D. J. (2005), ICESat validation of SRTM C-band digital elevation models, Geophys. Res. Lett., 32, L22S01, doi:10.1029/2005GL023957.

Carabajal, C. C., & Harding, D. J. (2006), SRTM C-Band and ICESat Laser Altimetry Elevation Comparisons as a Function of Tree Cover and Relief, Am. Soc. Photogram. Rem. Sens., 72(3), 287–298.

Chen, C. W. and Zebker, H. A., "Two-dimensional phase unwrapping with use of statistical models for cost functions in nonlinear optimization," J. Opt. Soc. Amer. A, vol. 18, pp. 338–351, 2001.

Danielson, J.J., and D.B. Gesch, 2011, Global Multi-resolution Terrain Elevation Data 2010 (GMTED2010). U.S. Geological Survey Open-File Report 2011-1073.

Farr, T., Rosen, P., Caro, E., Crippen, R., Duran, R., Hensley, S., Kobrick, M., Paller, M., Rodriquez, E., Roth, L., Seal, D., Schaffer, S., Shimada, J., Umland, J., Werner, M., Oskin, M., Burbank, D., & Alsdorf, D. (2007), The Shuttle Radar Topography Mission, Reviews of Geophysics, Vol. 45, 1-33, RG2004, Paper 2005RG000183.

Fricker, H. A., Borsa, A., Minster, B., Carabajal, C., Quinn, K., & Bills, B. (2005). Assessment of ICESat performance at the salar de Uyuni, Bolivia. Geophysical Research Letters, 32.

Fujisada, H., M. Urai, and A. Iwasaki, 2011, Advanced methodology for ASTER DEM generation. IEEE Transactions on Geoscience and Remote Sensing, v. 49, no. 12, p.5080-5091.

Fujisada, H., M. Urai, and A. Iwasaki, 2012, Technical methodology for ASTER Global DEM. IEEE Transactions on Geoscience and Remote Sensing, v. 50, no. 10, p.3725-3736.

Gallant, J., & Read, A. (2009). Enhancing the srtm data for australia. In Proc. Geomorphometry (pp. 149-154). Zurich, Switzerland.

Goldstein, R. M., Zebker, H. A., and Werner, C. L., "Satellite Radar Interferometry: Two-Dimensional Phase Unwrapping," Radio Science, vol. 23, pp. 713-720, Jul. 1988.

Gonzalez, J., Bachmann, M., Krieger, G., & Fiedler, H. (2010). Development of the TanDEM-X calibration concept: Analysis of systematic errors. IEEE Transactions on Geoscience and Remote Sensing, 48 , 716-726.

Grohman, G., G. Kroenung, and J. Strebeck, 2006, Filling SRTM voids: The delta surface fill method. Photogrammetric Engineering and Remote Sensing, v. 72, no. 3, pp. 213-216.

Hensley, S., Munjy, R., & Rosen, P. A. (2001). Interferometric synthetic aperture radar, digital elevation model technologies and applications: The dem users manual (d. f. maune, ed.). chapter 6. (pp. 142-206). ASPRS.

Krieger, G., Moreira, A., Fiedler, H., Hajnsek, I., Werner, M., Younis, M., & Zink, M. (2007). TanDEM-X: a satellite formation for high-resolution SAR interferometry. IEEE Transactions on Geoscience and Remote Sensing, 45 , 3317-3341.

Lefsky, M. (2010). A global forest canopy height map from the Moderate Resolution Imaging Spectroradiometer and the Geoscience Laser Altimeter System. Geophys. Res. Lett., 37, L15401.

Meyer, T. H. (2010). Introduction to geometrical and physical geodesy: foundations of geomatics. (1st ed.). Redlands, California: ESRI Press.

Neuenschwander, A. L., Urban, T. J., Gutierrez, R., & Schutz, B. E. (2008). Characterization of ICESat/GLAS waveforms over terrestrial ecosystems: Implications for vegetation mapping. Journal of Geophysical Research: Biogeosciences, 113.

Neumann, M., Ferro-Famil, L., & Reigber, A. (2010). Estimation of forest structure, ground and canopy layer characteristics from multi{baseline polarimetric interferometric SAR data. IEEE Transactions on Geoscience and Remote Sensing, 48 , 1086-1104.

NGA (2003). SRTM Water Body Data Product Specific Guidance. Version 2.0.

Peckham, S. D., Profile, Plan and Streamline Curvature: A Simple Derivation and Applications, Geomorphometry 2011 Conference, Redlands, California, September 7-9, 2011, http://geomorphometry.org/Peckham2011a.

Rignot, E., Echelmeyer, K., & Krabill, W. (2001). Penetration depth of interferometric synthetic-aperture radar signals in snow and ice. Geophysical Research Letters, 28 , 3501-3504.

Rodriguez, E., Morris, C. S., Belz, J. E., Chapin, E., Martin, J., Daffer, W., & Hensley, S. (2005), An Assessment of the SRTM Topographic Products, Technical Report JPL D-31639, Jet Propulsion Laboratory, Pasadena, California, 143 pp.

Rodriquez, E., Morris, C., & Belz, J. E. (2006), A global assessment of the SRTM performance, Photogram. Eng. and Rem. Sens., 72(3), 249–260.

Rosen, P. A., Hensley, S., Joughin, I. R., Li, F. K., Madsen, S. N., Rodriguez, E., & Goldstein, R. M. (2000). Synthetic Aperture Radar Interferometry. Proc. IEEE, 88, 333-382.

Sauber, J., Molnia, B., Carabajal, C., Luthcke, S., & Muskett, R. (2005). Ice elevations and surface change on the malaspina glacier, alaska. Geophysical Research Letters, 32, 14.

Savitzky, A., & Golay, M. J. E. (1964). Smoothing and Differentiation of Data by Simplified Least Squares Procedures. Analytical Chemistry, 36, 1627-1639.

Simard, M., Pinto, N., Fisher, J. B., & Baccini, A. (2011). Mapping forest canopy height globally with spaceborne lidar. Journal of Geophysical Research: Biogeosciences, 116.

Simard, M., Neumann, M., & Buckley, S.M. (2016), Validation of the New SRTM Digital Elevation Model (NASADEM) with ICESAT/GLAS over the United States, In the Proceedings of the International Geoscience and Remote Sensing Symposium, Beijing, China, July 10-15, 2016.

Slater, J. A., G. Garvey, C. Johnston, J. Haase, B. Heady, G. Kroenung, and J. Little, 2006, The SRTM data 'finishing' process and products. Photogrammetric Engineering and Remote Sensing, 72, 237–247.

Smith, B., & Sandwell, D. (2003). Accuracy and resolution of shuttle radar topography mission data. Geophysical Research Letters.

Tadono, T., H. Nagai, H. Ishida, F. Oda, S. Naito, K. Minakawa, and H. Iwamoto, 2016, Generation of the 30m-mesh global digital surface model by ALOS PRISM. The International Archives of the Photogrammetry, Remote Sensing and Spatial Information Sciences, ISPRS, Volume XLI-B4, pp.157-162.

Tierney, C. C., Kantha, L. H., & Born, G. H. (2000). Shallow and deep water global ocean tides from altimetry and numerical modeling. Journal of Geophysical Research: Oceans, 105, 11259-11277.

Zwally, H. J., Schutz, B., Abdalati, W., Abshire, J., Bentley, C., Brenner, A., Bufton, J., Dezio, J., Hancock, D., Harding, D., Herring, T., Minster, B., Quinn, K., Palm, S., Spinhirne, J., & Thomas, R. (2002). ICESat's laser measurements of polar ice, atmosphere, ocean, and land, Journal of Geodynamics, 34, 405-445.